ČESKÉ VYSOKÉ UČENÍ TECHNICKÉ V PRAZE

Fakulta jaderná a fyzikálně inženýrská

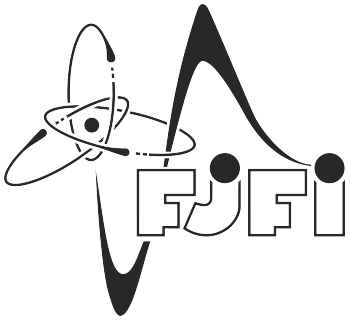

Rychle rozmítaný divertor potlačující tepelné pulzy v tokamacích

Fast swept divertor suppressing transient heat pulses in tokamaks

Diplomová práce/master's thesis

Autor/author: **Bc. Samuel Lukeš**
Vedoucí práce/supervisor: **Res. Prof. Jan Horáček, dr. és. sc.**
Akademický rok/academic year: 2021/2022

Čestné prohlášení:

Prohlašuji, že jsem svou diplomovou práci vypracoval samostatně a použil jsem pouze podklady (literaturu, projekty, SW atd....) uvedené v přiloženém seznamu.

Nemám závažný důvod proti použití tohoto školního díla ve smyslu § 60 Zákona č. 121/2000 Sb., o právu autorském, o právech souvisejících s právem autorským a o změně některých zákonů (autorský zákon).

V Praze dne 2. 5. 2022 Samuel Lukeš

Poděkování:

Děkuji zejména Res. Prof. Jan Horáček, dr. és sc. za jeho vedení a spolupráci na mé diplomové práci, ochotě pomoci kdykoliv bylo třeba a snahu o mé začlenění do vědecké komunity pomocí vedlejších projektů.

Dále děkuji Ing. Jakub Cikhardt, Ph.D. za jeho rady v oblasti vysokoproudé elektrotechniky, panu Matouš Lorenc ze společnosti HUMUSOFT s.r.o., který mi pomohl v mých začátcích se softwarem COMSOL Multiphysics a Ústavu fyziky plazmatu AV ČR, že mi byla umožněna práce na jejich výpočetních klusterech s licencí pro COMSOL Multiphysics, a že mi bylo v rámci těchto simulací vždy vyhověno.

Nakonec děkuji i své rodině a nejbližším, kteří mě pomáhali po celou dobu mých studií.

Název práce:

Rychle rozmítaný divertor potlačující tepelné pulzy v tokamacích

Autor: Bc. Samuel Lukeš

Studijní program: Fyzika plazmatu a termojaderné fúze

Druh práce: Diplomová práce

Vedoucí práce: Res. Prof. Jan Horáček, dr. és sc.,
Ústav fyziky plazmatu AV ČR, v.v.i.

Abstrakt: Navzdory tomu, že magneticky udržená termonukleární fúze je díky nově budovaným a plánovaným reaktorům stále realističtější, jedna z osmi zbývajících výzev, přežití tepelného štítu chránící vakuovou komoru reaktoru (tvaru tokamaku) před plazmatem, stále hledá řešení. Jedna z nestabilit plazmatu, Edge Localized Mode (ELM), je pravidelný tepelný puls výrazně ničící tepelný štít. Navrhujeme nový koncept magnetického rozmítání kontaktního bodu plazmatu se štítem (strike-point) dostatečně rychle a daleko, aby se rozložilo tepelné zatížení. Demonstrujeme proveditelnost takového systému specializovaných měděných cívek nacházející se přímo ve vakuové komoře a připojených k rezonančnímu obvodu, včetně indukovaných proudů a výkonové elektroniky, pro EU DEMOnstrační fúzní elektrárnu (EU DEMO). Naše simulace poskytují požadované rozmítání strike-pointu při frekvenci 1 kHz, čímž se potlačuje nárůst povrchové teploty vyvolaný ELM faktorem 3. Když se rozmítání sloučí s jinými známými koncepty zmírnění tepelného toku, ELM by mohly být zmírněny natolik, aby se zajistil bezpečný provoz EU DEMO při módu s vyšším udržením energie.

Klíčová slova: tokamak, termonukleární plazma, EU DEMO, divertor, materiál a tepelné šoky, ELM nestability a jejich mititgace, rezonanční obvod, vysokoproudé systémy

Title:

Fast swept divertor suppressing transient heat pulses in tokamaks

Author: Bc. Samuel Lukes

Abstract: Despite the fact that magnetic thermonuclear fusion is becoming more and more realistic through newly built and planned reactors, one of eight remaining challenges, survival of its heat shield protecting the reactor tokamak vacuum vessel against plasma, is still looking for a solution. One of plasma instabilities, Edge Localized Mode (ELM), is a heat pulse significantly destroying the heat shield. We propose a novel concept of magnetic sweeping of the plasma contact strike point fast and far enough in order to spread the heat loads. We demonstrate feasibility of such system of dedicated in-vessel copper coils connected to a resonant circuit, including the induced currents and power electronics for EU DEMOnstration fusion power plant (EU DEMO). Our simulations yields the desired strike point sweeping at 1 kHz frequency, suppressing the ELM-induced surface temperature rise by a factor of 3. When multiplied by another known mitigation concepts, ELMs might be mitigated enough to ensure safe high-confinement operation of EU DEMO.

Key words: tokamak, thermonuclear plasma, EU DEMO, divertor, material and thermal shocks, ELM instabilities and their mitigation, resonant circuit, high-current systems

During my studies, I contributed to several research papers:

as the first author:

- S. Lukes, J. Horacek, V. Veselovsky, P. Vondracek, D. Sestak, J. Adamek, V. Weinzettl and I. Duran: *Conceptual design of reciprocating probes and material-testing manipulator for tokamak COMPASS Upgrade*, Journal of Instrumentation, 17(02), C02007 (2022): https://doi.org/10.1088/1748-0221/17/02/c02007

  - Three new in-vessel manipulators for COMPASS Upgrade tokamak are designed. Thanks to the optimization of older concepts, deep reciprocation of electrostatic probes near separatrix should be possible. For the material-testing manipulator with an inclination capability we predict to reach EU DEMO relevant heat fluxes, even survive if liquid metal target is used. I mainly contributed via the implementation of 1D heat conduction code with a simple motion solver used for the optimization of several springs described in the paper. Also actively contributed to the main design of all three manipulators and worked on several add-on ideas for a much wider usability of the manipulators themselves.

as a co-author:

- J. Horacek, S. Lukes, J. Adamek, J. Havlicek, S. Entler, J. Seidl, J. Cavalier, J. Cikhardt and V. Sedmidubsky: *Novel concept suppressing plasma heat pulses in a tokamak by fast divertor sweeping.* Submitted to journal Nature Physics as NPHYS-2022-04-01087.

  - Unmitigated high confinement edge localized mode (ELM) is a regular heat pulse destroying the heat shield. We suggest a concept of magnetic sweeping of the plasma contact strike point fast and far enough in order to spread the heat of future tokamak ELMs. **As this paper is the main output of the same project as my thesis, I describe here only the work mainly done by myself and, if needed, further research is referenced to this paper.**

- M. Hron, et al.: *Overview of the COMPASS results*, 2021 Nucl. Fusion in press: https://doi.org/10.1088/1741-4326/ac301f

- J. Horacek, et. al.: *Predictive modelling of liquid metal divertor: from COMPASS tokamak towards Upgrade.* Phys. Scr. 96 124013 (2021): https://doi.org/10.1088/1402-4896/AC1DC9

- J. Horacek, et. al.: *Modeling of COMPASS tokamak divertor liquid metal experiments.* Nuclear Materials and Energy 25:100860 (2020): https://doi.org/10.1016/j.nme.2020.100860

and collaborated on other research tasks:

- Temperature evolution analysis of a new rail-probe diagnostic system for COMPASS Upgrade tokamak. Supervised by Mgr. Jiří Adámek, Ph.D. and results are expected to be published in 2022 in Review of Scientific Instruments or Journal of Instrumentation.
- D. Tskhakaya, S. Lukes and M. Komm: *Test Particle Simulations for ITER Lost Alpha Monitor*. Final report for the project: ITER CONTRACT NUMBER – IO/21/CT/4300002322, Project reference: IO/20/RFQ/10020238/BBE
- S. Lukes, et. al.: *Využití jevu vířivých proudů k usměrnění vysokofrekvenčního magnetického pole*. [online], [cited 1.3.2022], Available from: http://golem.fjfi.cvut.cz/wiki/TrainingCourses/FTTF/2020-2021/SamuelLuk/index

COMSOL Multiphysics

I have been given an opportunity to learn COMSOL Multiphysics software mainly via the licensing of Institute of Plasma Physics of the CAS. COMSOL Multiphysics is a cross-platform finite element analysis, solver and multiphysics simulation software, which offers widespread support and very user-friendly environment. It offers many add-on modules in the field of electromagnetism, structural mechanics, acoustics, fluid flow, heat transfer and chemical engineering. The biggest advantage of COMSOL is its capability of solving multi-physical problems and parallelization methods when used on computational clusters, which I used several times for a variety of different topics:

- The most I learned during simulations for the project of my thesis, where AC/DC module is used.
- 2D and 3D Heat Transfer with Surface-to-Surface Heat Radiation simulations for the rail-probe temperature evolution analysis during operation of COMPASS Upgrade tokamak.
- Structural Mechanics in a simple truss support table analysis of a heavy reciprocating probe mechanism for COMPASS Upgrade tokamak.
- An analysis of induced $J \times B$ force acting on such probe during its movement has also been made via the AC/DC module.

My thesis directly follows Richard Duban's master's thesis, FNSPE CTU 2017

- R. Duban: Study of New Technique for Distribution of Tokamak Divertor Plasma Heat Flux by Fast Swept Magnetic Coil. Master's thesis, Czech Technical University, FNSPE, Prague, 2017
  - Thematically similar work has been done before. Unfortunately, during further research, new obstacles were found (interaction of high-frequency magnetic field with a conductive vessel of tokamak, influence of a flight time of ions from midplane to divertor, absence of suitable components, etc.), which are further solved in my thesis. Nevertheless, I found a lot of useful information there that I continued to work with.

Table of contents

1 Introduction

Today's world is increasingly aware of its dangerous dependence on fossil fuels. Their ever-increasing consumption is not sustainable in the long run. Even though there are still being found new deposits and new ways how to get fuel (for example: shale gas extraction [1] or methane hydrate extraction from the ocean floor [2]), their combustion still produces greenhouse gases and smoke, which adversely affects human health, implicate long-term climate changes and dependence of the European Union on politically unfriendly countries.

Despite all the efforts of the modern world to reduce its dependence on fossil fuels, their combustion still represents $\sim 85\%$ of global primary energy consumption. Compensation in the form of current renewable resources (solar, wind, hydro, geothermal, ...) often depends on the weather, day/night cycle, season and location. Its usage is limited in the Czech Republic below $1/4$ of the year due to absence of large-enough electric storage. As a result, it reduces their land use performance, which is already significantly lower than that of fossil fuels. A rescue was offered by fission nuclear energy at the beginning of the second half of the 20th century, but it has been stagnant for 50 years due to a negative public response due to world-famous fission power plant accidents.

Fusion energy appears to be a solution in form of an inexhaustible and, in addition, safe source of green energy with acceptable economics [3]. Unfortunately, for 70 years, humanity has not yet succeeded in building a power plant that would be able to compete with other sources in terms of efficiency. All this could be changed by International Thermonuclear Experimental Reactor (ITER) [4], which is to act as an energy amplifier with an amplification of $Q = 10$ of input energy, reaching a fusion power output of 500 MW in 2035. We expect the first European DEMOnstration power plant (EU DEMO) with a useful heat output of > 2 GW to be built by 2060, according to Fusion Energy Roadmap from 2018 [5].

While the construction of ITER is in full swing, thanks to its larger parameters, DEMO design is still being developed. The most crucial for its design will be the results from ITER, to which it should in principle be very similar. However, some problems can be predicted today. In this work, a system that solves one of eight main problems of DEMO [6], namely survival of solid shield targets by high thermal pulses of thermonuclear plasma, will be presented.

2 Overview

2.1 Thermonuclear fusion

2.1.1 Principle

The human body is dependent on obtaining energy from food. Food contains sugar molecules that the body is chemically able to rearrange into other molecules or arrangements. However, each different interacting arrangement of atomic particles has a different binding energy, which manifests itself as a slight change in mass of all considered particles, according to known Einstein's relationship between the energy E and the mass m

$$E = m \cdot c^2 \quad [7], \tag{1}$$

where $c = 2.998 \cdot 10^8$ m/s is speed of light propagation in vacuum [8]. Thus, if the arrangement of the sugar molecule in the body has a lower overall weight than before, energy is released. The same principle works, for example, in combustion of fossil fuels, where carbon atom C and two oxygen atoms O have a greater mass than carbon dioxide molecule CO_2. Excess energy is transferred to kinetic energy of CO_2 during the process, which manifests itself as heat on a macroscopic scale. Nuclear fusion uses $\sim 10^7\times$ greater difference in binding energies per particle than is possible by chemical reactions.

The current favorite seems to be a fusion of hydrogen isotope ions: deuterium ${}^2_1\mathrm{H}^+$ (D^+) and tritium ${}^3_1\mathrm{H}^+$ (T^+), which has the largest effective cross-section (probability of merging) of all considered. The D-T fusion scheme looks like this

$$\mathrm{D}^+ \quad + \quad \mathrm{T}^+ \quad = \quad {}^4_2\mathrm{He}^{2+} \quad + \quad {}^1_0\mathrm{n} \quad + \quad 17.6\ \mathrm{MeV}. \tag{2}$$

But conditions for achieving it are at our current technological limits. To overcome repulsive electrical forces between charged ions extreme temperatures are needed. On the other hand, maximum temperature is limited by a requirement for the greatest possible energy gain. The most suitable conditions for efficient D-T fusion are between 10 keV and 20 keV (or $116 \cdot 10^6$ to $232 \cdot 10^6$ K, for comparison, temperature in the Sun's core is only $16 \cdot 10^6$ K). No solid material is able to withstand such temperatures, and therefore current efforts of research projects are mainly focused on finding the most suitable way to maintain and separate the plasma from the rest of the fusion power plant.

2.1.2 Plasma

It is important to realize that any substance is in a state called plasma at these temperatures. It is a state in which particles of matter are so energetic that they ionize themselves via collisions (the ionization energy of hydrogen is 13.6 eV, which corresponds

to a temperature of 160,000 K) or via already free electrons accelerated by an external electric field. Released electrons have a possibility of a free movement around the cluster of positively charged atomic nuclei. Thus, the plasma appears macroscopically neutral in the same way as a substance from which it originated. But thanks to the free movement of charged particles relative to each other, currents can be induced in the plasma (similar to metals, but ions can also conduct current in the plasma), even trapping the particles using magnetic fields, therefore sustaining the plasma in desired volume.

The cause is so-called Lorentz force $\mathbf{F}_\mathrm{L}$, which acts on any particle with electric charge q and velocity $\mathbf{v}$ in a electric field $\mathbf{E}$ and a magnetic flux density $\mathbf{B}$

$$\mathbf{F}_\mathrm{L} = q\mathbf{E} + q\mathbf{v} \times \mathbf{B} \quad [9] \tag{3}$$

While the first term $q\mathbf{E}$ drives the particle in $\mathbf{E}$ direction and thus forms a current in the plasma, the second member $q\mathbf{v} \times \mathbf{B}$ acts perpendicular to both the movement of the particle $\mathbf{v}$ and direction of the magnetic field $\mathbf{B}$.

If we neglect the first term $q\mathbf{E}$ (can cause drifts of resulting trajectories and/or increasing $\mathbf{v}$ in the direction of $\mathbf{B}$) and consider a homogeneous magnetic field in a direction of x-axis, $\mathbf{B} = (B; 0; 0)$, we can derive a trajectory of the particle with mass m with respect to its initial velocity $\mathbf{v}(0) = (v_{x0}; v_{y0}; v_{z0})$. According to the second Newton's law of motion

$$m\frac{\partial^2 \mathbf{r}}{\partial t^2} = m\frac{\partial \mathbf{v}}{\partial t} = \mathbf{F}_\mathrm{L}^\mathrm{magnetic} = q\mathbf{v} \times \mathbf{B} \quad [10], \tag{4}$$

where $r = (x; y; z)$ is a position of the particle starting from $r(0) = (x_0; y_0; z_0)$ and t stands for time. After writing the vector equation in scalar form

$$\frac{\partial^2 x}{\partial t^2} = 0 \tag{5}$$

$$\frac{\partial^2 y}{\partial t^2} = \frac{qB}{m} \cdot \frac{\partial z}{\partial t} \tag{6}$$

$$\frac{\partial^2 z}{\partial t^2} = -\frac{qB}{m} \cdot \frac{\partial y}{\partial t}, \tag{7}$$

we can guess a result to be in a form of

$$x(t) = X_1 t + X_2 \tag{8}$$

$$y(t) = Y_1 \sin(Y_2 t + Y_3) + Y_4 \tag{9}$$

$$z(t) = Z_1 \cos(Z_2 t + Z_3) + Z_4 \tag{10}$$

x-component can derived easily by assuming initial conditions

$$x_0 = x(0) = X_2 \tag{11}$$

$$v_{x0} = v_x(0) = \left(\frac{\partial x}{\partial t}\right)(0) = X_1 \tag{12}$$

In order to find the constants of the other two equations we first substitute them into the original equations

$$-Y_1 Y_2^2 \sin(Y_2 t + Y_3) = -\frac{qB}{m} \cdot Z_1 Z_2 \sin(Z_2 t + Z_3) \tag{13}$$

$$-Z_1 Z_2^2 \cos(Z_2 t + Z_3) = -\frac{qB}{m} \cdot Y_1 Y_2 \cos(Y_2 t + Y_3) \tag{14}$$

Because the equations must hold at all times t, it must hold that

$$Y_2 = Z_2 = B_2 \quad \text{and} \quad Y_3 = Z_3 = C_3 \tag{15}$$

With these conditions, we can shorten the equations

$$Y_1 B_2 = \frac{qB}{m} \cdot Z_1 \tag{16}$$

$$Z_1 B_2 = \frac{qB}{m} \cdot Y_1 \tag{17}$$

and see that

$$Y_1 = Z_1 = A_1, \quad \text{therefore} \quad B_2 = \frac{qB}{m} \tag{18}$$

Finally, the initial conditions remain

$$y_0 = y(0) = A_1 \sin(C_3) + Y_4 \qquad v_{y0} = v_y(0) = \left(\frac{\partial y}{\partial t}\right)(0) = A_1 \frac{qB}{m} \cos(C_3) \tag{19}$$

$$z_0 = z(0) = A_1 \cos(C_3) + Z_4 \qquad v_{z0} = v_z(0) = \left(\frac{\partial z}{\partial t}\right)(0) = -A_1 \frac{qB}{m} \sin(C_3) \tag{20}$$

Solving the velocity equations we get

$$v_{y0}^2 + v_{z0}^2 = \left(A_1 \frac{qB}{m} \cos(C_3)\right)^2 + \left(-A_1 \frac{qB}{m} \sin(C_3)\right)^2 = \left(A_1 \frac{qB}{m}\right)^2 \tag{21}$$

$$A_1 = \sqrt{v_{y0}^2 + v_{z0}^2} \frac{m}{|q|B} = v_{\perp 0} \frac{m}{|q|B} \tag{22}$$

Because time evolution of $v_{y,z}$ is only harmonic, $v_{\perp 0} = v_\perp$. C_3 is a constant phase shift depending only on the initial values, such as the constants Y_4 and Z_4, and are not important for us. The harmonic evolution of coordinates y, z and velocities $v_{y,z}$ shifted by 90° results into a circular motion of radius $r_\mathrm{L} = \frac{v_\perp m}{|q|B}$, called *Larmor radius*, and angular frequency $\omega = \frac{|q|B}{m}$. Assuming the constant velocity in the x-direction we obtain a helical trajectory.

If we approximate non-homogeneous magnetic field as being composed of homogeneous fields "glued" together by some error fields we can say that the particle follows the magnetic field line (slightly different in each of homogeneous fields) around which it orbits. When studying even the "error" fields we would find that it causes jumps of the particle to a different field line, these jumps represent themselves as necessary drifts of the original trajectory.

This way of keeping an extremely hot and ionized mass in a vacuum, in principle, independently of its surroundings, led many scientists in the middle of the 20th century to come up with many ideas on how to build a fusion reactor. In the late 1950s, the world recognized that Russian device called tokamak is the most suitable.

2.1.3 Tokamak

So far, the most successful fusion reactors are stars. To fuse hydrogen atoms into helium they use their enormous gravitational forces, which we are unable to imitate on Earth. But, as noted in section 2.1.2, in the middle of the 20th century, magnetic force proved to be an option for maintaining an extremely hot plasma in terrestrial conditions. Scientists around the world have come up with various device concepts (Z-pinch, θ-pinch, linear magnetic mirrors, inertial fusion, fusor, ...), but they all failed to release more energy than they consumed. Among all these designs, a tokamak device has proven to be very successful in scaling these energy conditions to larger and larger copies of itself.

Tokamak, or toroidal vessel with magnetic coils, serves to sustain a discharge at thermonuclear temperatures and to understand both plasma and thermonuclear fusion. The plasma discharge is confined inside a toroidal vacuum vessel (filled with working gas, i.e. mostly hydrogen and/or its isotopes) by system of coils (see Figure 1) generating strong magnetic **B** and electric **E** fields reaching several Tesla and inducing currents even up to 100 kA/m^2.

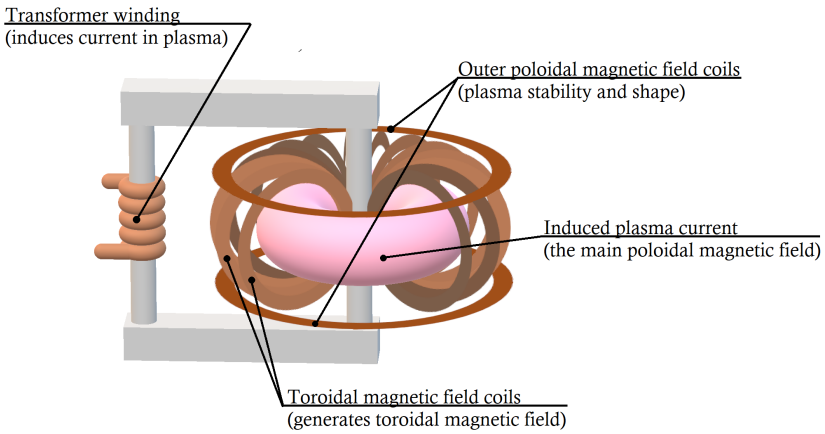

Figure 1: *Basic arrangement of magnetic coils of every tokamak.*

The central solenoid (in older designs a ferritic transformer core was used) induces a toroidal current in the plasma, which heats the plasma, but only up to ~ 1 keV. Higher temperatures are achieved by means of additional heating systems, beams of neutral particles or microwave electromagnetic waves. Distribution of the induced current density creates a pressure gradient which results in the highest plasma density on axis of the torus. But only a combination with the toroidal magnetic field coils creates a helical magnetic field, which cancels the otherwise necessarily emerging $\mathbf{E} \times \mathbf{B}$ drift of particles from the center of the torus. As a result, all electrically charged particles remain on helical trajectories along the magnetic field lines. However, the plasma current creates such a magnetic field which necessarily tries to stretch the current loop to a straight line. Therefore, the outer coils of the poloidal magnetic field, which compensate the force, must not be missing in the tokamaks either. The poloidal field coils also stabilize the plasma vertically/horizontally and optimize its shape.

In order to better stabilize and purify the plasma, many tokamaks began to use a so-called *D-shape* and *X-point*. It is a shape of the magnetic configuration in poloidal cross section, see Figure 2. The *D-shape* serves to balance the particle ratio in the vessel, because the toroidal shape of the vessel has more particles on outside, on Low magnetic Field Side (LFS). The asymmetric letter "D" has a larger area (more particles) on inside of the torus, where the coils of toroidal field are closer to each other (HFS). The *D-shape* also allows a creation of the *X-point* (or more points) in which there is zero poloidal magnetic field. Particles, whose trajectory is radially further from the center of the plasma than the magnetic field line which crosses the *X-point*, have left the magnetic confinement and continue to a selected area into the divertor region. The limiting magnetic surface closing itself in the vessel is called the Last Closed Flux Surface (LCFS). Due to extreme velocities along the magnetic field lines, the flow of escaped particles is concentrated in two toroidal circles (*strike-points*, when viewed in poloidal cross section). This means that the divertor tiles must withstand immense heat fluxes in the order of 10^6 to 10^8 W/m^2.

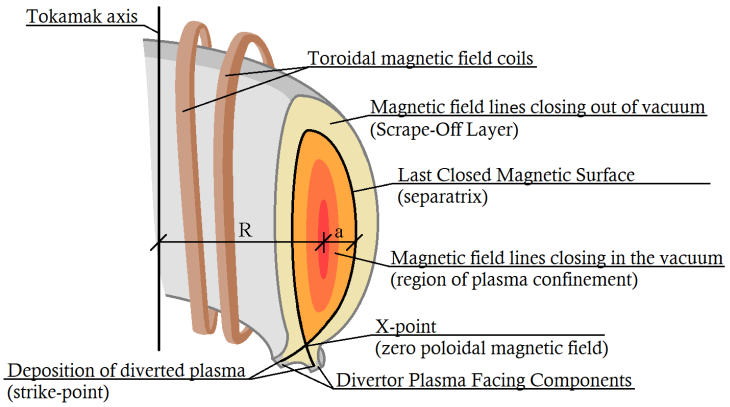

Figure 2: *Poloidal cross section of a tokamak vessel showing the D-shape plasma with the X-point and the strike-points.*

In plasma with *X-point* configuration, it is possible to switch from a standard Low confinement mode (L-mode) to a High confinement mode (H-mode) via the help of additional heating systems. *H-mode* was discovered by chance and offers $\sim 2\times$ or more better plasma confinement than *L-mode*. While in *L-mode*, diffusion of the particles from the plasma is dominated by fast turbulent structures, in *H-mode* there is such a large difference in plasma flows at its edge that they can significantly suppress the turbulence. Such suppression of diffusion results in a steeper increase in plasma parameters at its edge (*pedestal region*), see Figure 3

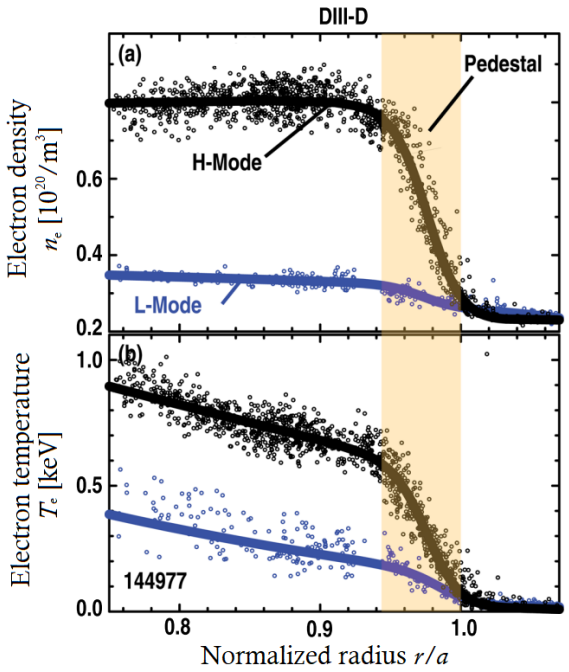

Figure 3: *Comparison of H-mode/L-mode edge profiles measured by Thomson scattering on DIII-D tokamak. Obtained and modified from [11].*

The success of the tokamak in the effectiveness of maintaining thermonuclear fusion is closely followed by similar device, stellarator. Instead of the induced current, it uses additional external coils to create the helical magnetic field. It is believed that its disadvantage lies only in engineering complexity of its design, which causes worse results for the same volume of plasma, but nowadays technologies are changing that. On the other hand, it would in principle allow for a continuous and safer (without plasma current instabilities) operation of a power plant, which in turn is a very complex matter for the tokamak (in principle an inductive device). In future reactors, non-inductive heating is envisaged, which also would have the task of maintaining the constant current in the plasma. Thus, the central solenoid begins to be given more secondary functions in form of an initial breakdown and heating of the working gas. The first European DEMOnstration power plant (EU DEMO1) still relies on a pulse mode in form of 2 hours long plasma and 15 minutes long pause to reverse the polarity and start another discharge.

2.2 Plasma-divertor interaction

Despite the fact that in the volume of confined plasma the main events take place, which can very strongly influence its surroundings through radiating processes, electromagnetic inductions and especially thermal loads, in this work we will mainly focus only on plasma, which has already diffused through LCFS and is in the area called Scrape-Off Layer (SOL), see Figure 2.

2.2.1 Basic SOL model

To understand how plasma can be described in SOL, we will show the simplest model.

The magnetic field inside and outside LCFS does not differ much locally, the same rules for particle motion apply to the plasma in SOL as to the confined plasma. Particle flow density perpendicular to the magnetic field $\Gamma_\perp$ can be determined by the Fick's first law

$$\Gamma_\perp = -D_\perp \cdot \frac{\partial n}{\partial r} \tag{23}$$

Where n denotes the concentration of particles in perpendicular (radial) direction to the toroidal magnetic field r and $D_\perp$ stands for the diffusivity. In real tokamak plasma there are other transport mechanisms such as drifting turbulent blobs, which are not proportional to the density gradient ∇n, so $D_\perp$ can serve here only as a rough estimation of reality. Inconsistency between theory and experiments led to high hopes in the early days of fusion research, but $D_\perp$ turned out to rather follow experimentally measured Bohm diffusion coefficient for magnetized plasmas $D_\mathrm{B} \sim B^{-1}$, which is orders of magnitude higher than the firstly expected classical diffusion coefficient $D_\mathrm{classic} \sim B^{-2}$. And such large particle/energy loss is the main reason why we, so far, can not maintain energy-efficient thermonuclear plasma in power plants smaller than ITER.

We see the radial difference in closed (inside LCFS) and open (outside LCFS) magnetic field only when we talk about the longitudinal flow of particles $j_\parallel$. The particles, as we said in Section 2.1.2, flow along the field lines that in the open field intersects the tokamak vessel. The plasma comes into contact with the vessel in the divertor region. The longitudinal motion of particles is much looser than the perpendicular and is given only by the ion-sound velocity

$$c_\mathrm{s} = \sqrt{\gamma k_\mathrm{B} T / m} \tag{24}$$

for a given temperature T of particles with mass m. $k_\mathrm{B} = 1.381 \cdot 10^{-23}$ J/K is the Boltzmann constant [8] and γ is the adiabatic index of the plasma. Considering the same particle leakage throughout LCFS and a random longitudinal direction of the particles as they leave the plasma, the particle density profile $n(r)$ in SOL will be the same everywhere

around LCFS. But because the particle flow in one direction along LCFS increases and is balanced by the particle flow in the other direction, there exists the *stagnation point* approximately (in this model) on the side opposite to the *X-point*, where the resulting particle flow $\Gamma_{\parallel} = 0$, see Figure 4.

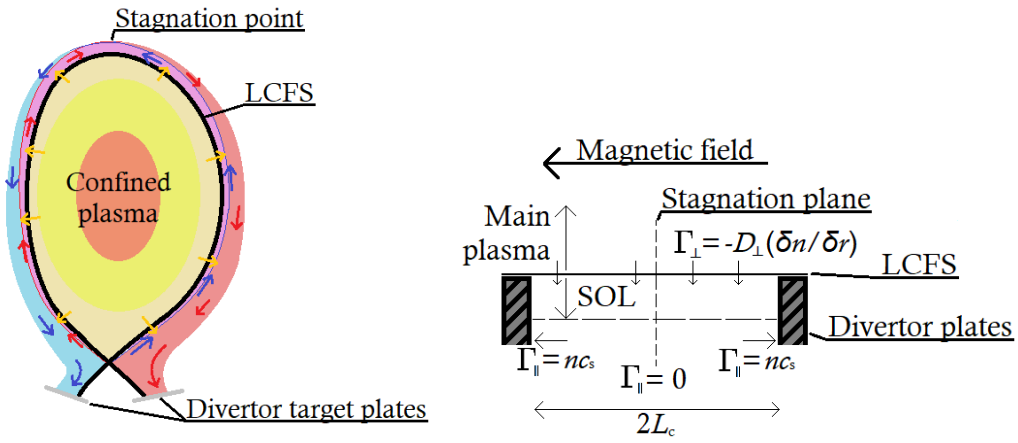

a) b)

Figure 4: a) *Poloidal cross-section of a tokamak showing a constant increase in particles along LCFS (yellow arrows) that can flow along or against the magnetic field (red, blue). Flows in both directions equalize at the stagnation point (in reality the stagnation point is localized way further on LFS due to higher particle losses on LFS).* b) *Basic SOL model scheme. The model is easier to understand when stretched along the magnetic field lines located near LCFS.*

We also need to know the longitudinal distance the particles can travel before impact. We need to realize the helical shape of the magnetic field in the tokamak. If the particle orbits in poloidal direction $N = 1$ times around the plasma, it orbits $M \geq 2$ (plasma stability limit) in toroidal direction. The ratio of these orbits is called the *safety factor* q. If we start measuring the trajectory of the particle from the *stagnation point* before hitting the divertor target, it will offend the so-called *connection length*

$$L_\mathrm{c} \cong \pi q R \quad (L_\mathrm{c}^\mathrm{ITER} \approx 150 \text{ m}) \tag{25}$$

Now we only compare the particle losses from SOL given by $\Gamma_{\parallel}$ with the inflow of particles into SOL given by $\Gamma_{\perp}$

$$\frac{\partial}{\partial r}\left(D_\perp \frac{\partial n}{\partial r}\right) = \frac{n c_\mathrm{s}}{L_\mathrm{c}} \tag{26}$$

If we consider the independence of $D_\perp$ and c_s on r, we obtain

$$n(r) = n(a) \exp\left[-\frac{(r-a)}{\lambda_\mathrm{n}}\right] \tag{27}$$

where $\lambda_\mathrm{n} = \sqrt{D_\perp L_\mathrm{c}/c_\mathrm{s}}$ is the characteristic thickness of SOL in orders of 10^0 cm. The

electron heat balance can be considered in similar way leading to a temperature profile

$$T_{\mathrm{e}}(r) = T_{\mathrm{e}}(a) \exp\left[-\frac{(r-a)}{\lambda_{\mathrm{T}}}\right] \tag{28}$$

and thanks to that, the heat flux profile looks also similar

$$q_{\parallel}(r) \cong q_{\parallel}(a) \exp\left[-\frac{(r-a)}{\lambda_{\mathrm{q}}}\right] \tag{29}$$

Despite the fact that today, especially thanks to COMPASS tokamak [12], a rather double exponential (*near* to LCFS and longer *main*) $q_{\parallel}$ profile is considered

$$q_{\parallel}(r) = q_{\parallel}^{\mathrm{main}}(a)[\exp(-(r-a)/\lambda_{\mathrm{q}}^{\mathrm{near}}) + R_{\mathrm{q}}^{-1} \exp(-(r-a)/\lambda_{\mathrm{q}}^{\mathrm{main}})], \tag{30}$$

we see that the heat flux incident on the divertor targets can be described as the exponential decrease. This is the main reason why the mentioned narrow *strike-points* can be observed on the divertor targets, where surface temperature of the tiles often reaches $> 10^3$ °C and this work will try to reduce such temperature to acceptable values. Above, we presented the diffusion coefficient $D_{\perp}$ as a number that we would like to be as small as possible, but now, we see that the larger $D_{\perp}$ gets the lower the heat flux will be in the divertor region.

2.2.2 Edge Localized Modes

We have seen that the steady-state heat flux on divertor $q_{\perp}$ (perpendicular to surface of the divertor targets) turns out to be highly concentrated in space, but even so, in future power plants it is expected not to exceed the engineering limit $q_{\perp} \approx 16$ MW/m^2 for a swirl water cooling on ITER or the somehow better hypervapotron. Getting below this limit requires, however, nearly order of magnitude decrease (by radiation) of the power flowing towards divertor. A much bigger problem are events, where also concentration in time takes place. Such events are very fast, but brings much more energy, therefore called *transient heat events*. One type of such events is caused by a regular instability called Edge Localized Mode (ELM).

This short burst releases 3-10% of stored plasma energy, accompanies the discovery of H-mode for which it is typical and are the main reason why H-mode is less and less considered as the main operational regime of fusion power plants. Under certain conditions smaller and/or irregular ELMs may occur that have been given a variety of classifications [11]. This work is primarily concerned only on the larger Type-I ELMs that are of more serious concern for future devices. In Figure 5 we can see what is happening in *pedestal* during ELM. Before ELM, the energy of plasma accumulates at its edge, which is then released in a brief moment, decreasing n_{e} and T_{e} profiles.

By extrapolation from current devices, the impacting parallel ELM energy density $\varepsilon_{\parallel}$

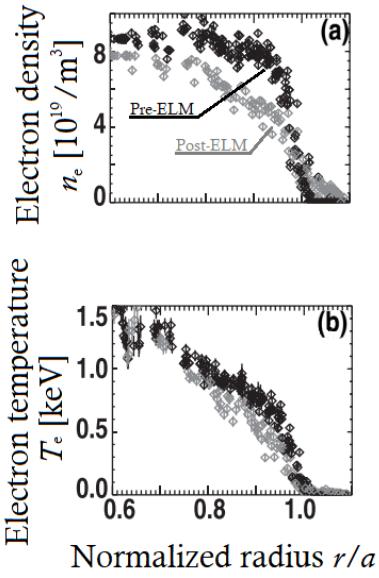

Figure 5: *Measured plasma pedestal profiles on DIII-D tokamak before ELM happens and after it happens. Obtained and modified from [11].*

can be estimated, see Figure 6. So-scaled prediction for ITER reaches $\varepsilon_{\parallel} = 15$ MJ/m^2. Even when mapped to the divertor target under shallow heat flux impact angle of 4.5°, it gets above tungsten recrystallization temperature $\approx 1,200$ °C (so strongly limiting its lifetime for cracking) but at least below melting (which was indeed observed on JET tokamak with deliberately high impact angle) [13]. It is clear that the problem will be even greater at larger EU DEMO.

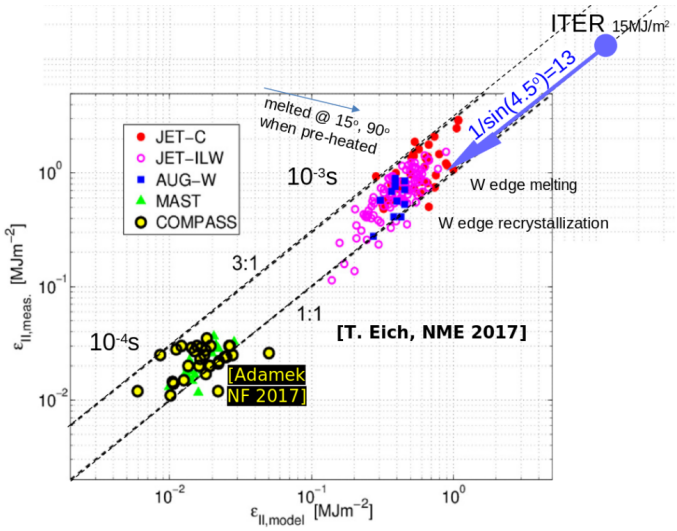

Figure 6: *Parallel ELM energy density $\varepsilon_{\parallel}$ measured against a modeled prediction. Graph also shows the characteristic times of ELMs $10^{-4} - 10^{-3}$ s, which are also important for comparing different thermal loads. Obtained and modified from [13].*

2.2.3 Other transient heat events

In tokamaks with divertor configuration other heat transients are possible, each with specific duration and heat load. They are often caused by a disruption. The tokamak disruption is a dramatic event in which the plasma confinement is suddenly lost. In a major disruption, it is followed by a complete loss of the plasma current. For example, the EU DEMO heat shock during an unmitigated disruption can exceed 100 $\mathrm{MJ/m^2/s^{1/2}}$, critically damaging the heat shield [14]. Sacrificial (one-use only) limiters are therefore considered to protect the vacuum vessel (see Figure 7), so the mitigation system presented here might be considered only as a reserve in such events.

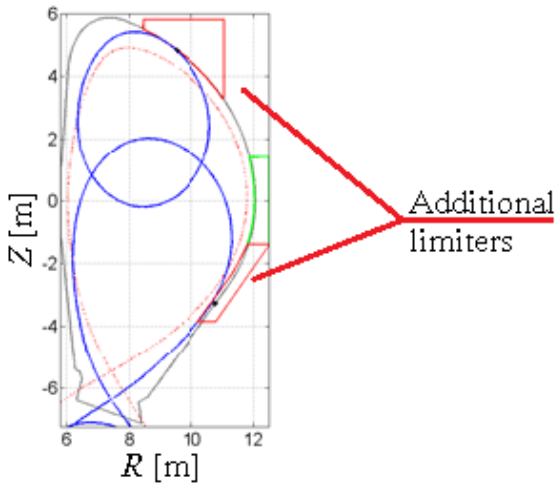

Figure 7: *EU DEMO limiter configuration for protection of First Wall (FW) during UP-VDE and DOWN-VDE. Obtained and modified from [15].*

The strongly elongated plasma configuration in ITER-like devices is vertically unstable unless an active control feedback at the vertical position is applied. A malfunction of this feedback system for variety of reasons can lead to a rapid plasma vertical displacement. As the plasma contacts the top or bottom of the vacuum vessel, the plasma current is rapidly forced to zero. The whole thermal energy of the plasma is expected to be lost at the contact point. This is called the Vertical Displacement Event (VDE) and is considered one of the worst possible events that will irreversibly damage the tokamak shield (evaporate a large part of the tungsten layer and endanger the cooling channels themselves) and can cause even worse accidents. Typical load for ITER is estimated as 60 $\mathrm{MJ/m^2}$ deposited in 500 ms [16].

2.2.4 Divertor shield and heat pulses

If we consider that the steady-state heat load is within the limits for the ITER-like tungsten divertor target, it is also necessary to keep the transient heat load below the tungsten thermal shock limit $\eta = 50$ $\mathrm{MJ/m^2/s^{1/2}}$ [17]. When exceeded, the affected part

of the shield melts. For EU DEMO and ITER it is expected to regularly happen due to ELMs when operating in H-mode, especially at the edges of the tiles due to finite ion orbit drifts. Comparing η with the previously mentioned values, we see the reason why transients are so dangerous for the long-term operation of a fusion power plant.

Even if η is not exceeded, it is important not to exceed the recrystallization temperature 1200 °C too many times, above which a significant reduction of the strength of tungsten was observed in the heat flux tests of divertors [18], and major cracks appear on its surface. This can, among other things, lead to plasma volume contamination by sputtered W ions. Even tiny fraction of 3×10^{-5} of W in the plasma increases by 20% the fusion limit (due to strong plasma radiation cooling), only for which a thermonuclear burn is possible [19].

2.2.5 Heat pulse mitigation techniques

Although there are many ways to effectively reduce the steady-state $q_{\perp}$, such as injecting a high proton number inert gas (Neon, Argon) into the divertor region to radiate as much incoming energy (*impurity seeding*) or periodically changing the *strike-point* position (described below in Section 2.4.1), none of them can reduce the Type-I ELM energy by a factor of 15 to 90 required for EU DEMO1 [17].

Many other methods directly targeting ELMs have achieved interesting results, but everyone is still awaiting results from ITER to see if the desired suppression takes place, how plasma confinement reacts to such systems and how reliable can they be. Among the most interesting are:

- Resonant Magnetic Perturbation (RMP) coils which with their additional radial magnetic field and real-time control feedback can fully stabilize the *pedestal* and completely prevent the formation of ELMs [20].
- ELM triggering via deuterium pellets does not suppress the total energy deposited by ELMs on the divertor targets but it increases their frequency so that the energy of individual ELMs is much lower. Since $\approx$ 5 mm pellets fired with frequencies 10-60 Hz for ITER are required [21], its long-term reliability could be an issue.
- Vertical "kicks", which also try to increase the frequency of ELMs, but using the system of vertical plasma stabilization, which is necessarily available to every tokamak [22].

More attractive solutions are plasma configurations which are naturally ELM-free. Among these, two candidates are of particular interest: the *Quiescent H-mode* (QH-mode) and the *Improved L-mode* (I-mode). Both regimes exhibit the noteworthy advantage of being naturally ELM free. However, both of them are quite poorly explored and understood in comparison to the standard ELMy H-mode configuration. As such, there are still

many open points which need to be carefully evaluated, both in terms of experiments and in terms of modelling, before anything can be concluded. R&D in present devices must be focused towards building knowledge on such regimes, namely to find operating boundaries, confinement and transition power scaling [23].

The last hope could also be a divertor shield made of liquid metals. Many experiments, most recently on COMPASS tokamak [24] and possibly in the future on COMPASS Upgrade tokamak [25], show its applicability. It is the use of low-melting metals (lithium, tin or their combinations) wetted in a capillary porous structure from high-melting metal (tungsten, molybdenum). The liquid metal forms a thin homogeneous layer on surface of the porous structure, which begins to evaporate under high thermal conditions. The fluid is stabilized by capillary forces, thanks to which it is also constantly replenished from a reservoir, so it is also possible to shape the target. When a certain heat load is reached, similarly to *impurity seeding*, generated metal vapor is so dense that a significant amount of incoming energy is radiated outside of the divertor.

Its main drawback is strong plasma impurity contamination which requires significant further research. More important to this work, because the target surface cooling by heat conduction is relatively negligible with respect to the cooling by vapor shielding and the vapor shielding even undesirably decreases when the dense plasma *strike-point* sweeps away from the hot vaporizing surface region, the liquid metal divertor is not suitable in combination with the fast sweeping technology described here.

2.3 EU DEMO

Although ITER (major radius $R = 6.2$ m, minor radius $a = 2.0$ m, plasma volume $V_\mathrm{p} = 840$ m^3) will be much larger than current largest tokamak JET ($R = 2.96$ m, $a = 1.25$ m, $V_\mathrm{p} = 100$ m^3), still it will be just a research reactor. Only its successor, the DEMOnstration power plant (DEMO), is to function as a full-fledged power plant. There are several proposals for DEMO around the world, but they are all waiting for experience from ITER. The same is true in European Union, whose proposal EU DEMO is the demonstration of technological and economic viability of fusion power operating with a closed tritium fuel cycle through the production of a few hundred MWs of net electricity to the grid. To achieve its goals, if utilizing a conventional tokamak design, EU DEMO reactor must have linear dimensions about 50% larger than ITER (see Figure 8), and a plasma density about 30% greater, which implies even larger heat loads on PFCs than on ITER.

On 25th November 2020 in Brussels, Belgium, the first project-wide gate review of EU DEMO project was completed by independent expert review panel. This gate is significant, not only as it marks the transition between the Pre-Conceptual Design Phase (2014 – 2020) and the Conceptual Design Phase (2021 – 2027), but also as it is the first time that a competent and experienced independent panel provides critical feedback to EU DEMO

Figure 8: *Planned development of tokamaks with the aim of achieving economically acceptable fusion energy. It is worth mentioning the just being launched Japanese tokamak JT-60SA, which should replace the function of the old JET tokamak by following a complementary research and development programme of future fusion power plants. Obtained and modified from [26].*

stakeholders. At present, work in Europe continues to be focused on the design of a pulsed DEMO plant concept, the so-called EU DEMO1, which is, unlike many other projects, the logical consequence of the most mature knowledge in physics (i.e. the H-mode scaling, exhaust, technology, ...) and so our work parameters are set to fit this project, see Table 1.

major radius R	9.0 m
minor radius a	2.6 m
on axis toroidal magnetic field B_{tor}	5.9 T
induced electrical current in plasma I_{p}	18 MA
mean electron temperature $< T_{\mathrm{e}} >$	12.6 keV
mean electron density $< n_{\mathrm{e}} >$	7.3×10^{-19} m^{-3}
"burning" plasma duration t_{burn}	2 h
fusion power output P_{fus}	2014 MW
net electricity output $P_{\mathrm{e,net}}$	500 MW
power flowing into the divertor region P_{div}	161 MW
blanket structure material	EUROFER 97
vacuum vessel material	AISI 316
low-temperature superconducting magnets material	Nb_3Sn (grading)
plasma facing components material	W
number of toroidal segments N	54

Table 1: *Overview of the main parameters for EU DEMO1. Data obtained from [23].*

One of the eight main challenges in EU DEMO proposal [23], called Key Design Integration Issues (KDIIs), is the wall/divertor protection to withstand plasma transients. Because even a small number of ELM events could cause serious damage to the tungsten divertor targets. In EU DEMO, a single Type-I ELM event will be sufficient to melt the

divertor target tungsten surface, and 50-100 unmitigated ELMs would result in the erosion of the entire target thickness [27]. As natural ELMs are foreseen with a frequency of ~ 1 Hz, many of ELM mitigation measures do not provide a credible solution for DEMO, and thus, unless a mitigation of ELM energy by a factor of 15 to 90 is found, it is very likely that the ELMy H-mode cannot be used as plasma operating regime in EU DEMO (this is perhaps true also for ITER). In this work, we will demonstrate a new way to safely mitigate such ELMs.

2.4 Fast divertor sweeping

When we talk about divertor sweeping, we mean sweeping of the position of *strike-points* in poloidal direction along divertor Plasma Facing Components (PFCs). The total energy supplied by the plasma is then deposited over a larger area at a given moment, which leads to a decrease in surface temperature and more efficient cooling.

The first ideas, scaling and calculations of this innovative system are described in [28, 29, 30, 31]. Where no eddy currents induced in the conductive components of the divertor, especially the divertor shield, were originally considered. Their inclusion in [13, 32, 33] in the simplest possible geometry of the divertor shielding significantly changed the necessary parameters.

2.4.1 Slow divertor sweeping

A divertor sweeping on JET tokamak is used as a standard technique to mitigate the steady state heat flux. Sweeping at 4 Hz with an amplitude of 5.4 cm, they were able to reduce surface temperature of the tungsten divertor tiles by 50% in a JET 'hybrid' high performance ELMy H-Mode scenario with a heating power of $\sim$30 MW and a radiation power of $\sim$10 MW. Only thanks to the sweeping it was possible to maintain this discharge for the whole 5 s [34]. A similar sweep is considered as an emergency option (or concurrently) in the event of a sudden loss of plasma detachment on reactor-class tokamaks such as EU DEMO [35] or SPARC [36]. Specifically for EU DEMO, a sweep of 20 cm/1 Hz is considered when a sudden increase in the steady state heat flux to $\sim$15 MW/m^2 happens. This will reduce the peak heat flux to cooling by a factor of ~ 4 and reduce the tungsten shield surface temperature by a factor of 2. In the case of long term steady-state use, 4 Hz sweeping is considered.

This "slow" sweeping magnetic field is excited by the outer poloidal field coils, the frequency of which is limited to a few Hz due to induced eddy currents that do not allow the field to penetrate through the conductive vacuum vessel. However, for sweeping to be effective for transient heat pulses, it is necessary to increase the frequency up to several kHz, therefore we call it the "fast" sweeping.

2.4.2 Sweeping system layout

In [13], the coil system is described as a C-shaped solenoid that will be placed in each of the 54 DEMO divertor cassettes, see Figure 9a. Each of the cassettes would have to contain two such coils, one for the *strike-point* on LFS (outer *strike-point*) and one for the *strike-point* on HFS (inner *strike-point*). The coils must be placed as close to the plasma as possible to maximize their efficiency. But at the same time they must be in substantial occlusion at least behind the Plasma Facing Components (PFCs). PFCs themselves will be significantly segmented due to thermal expansion and induced currents from the plasma instabilities, but their steel support structure must be solid. Therefore, the work assumes a toroidal placement of the coils in the necessary gaps between the individual divertor cassettes, but even so, the damping eddy currents in the structure are not negligible. In [13], there is considered a hole (10 cm in diameter) in the PFC, so the coil mouth must settle far enough from the possible position of the *strike-point* to prevent the edges of the hole from melting. The hole must be filled with a non-conductive plasma-facing material, such as boron-nitride.

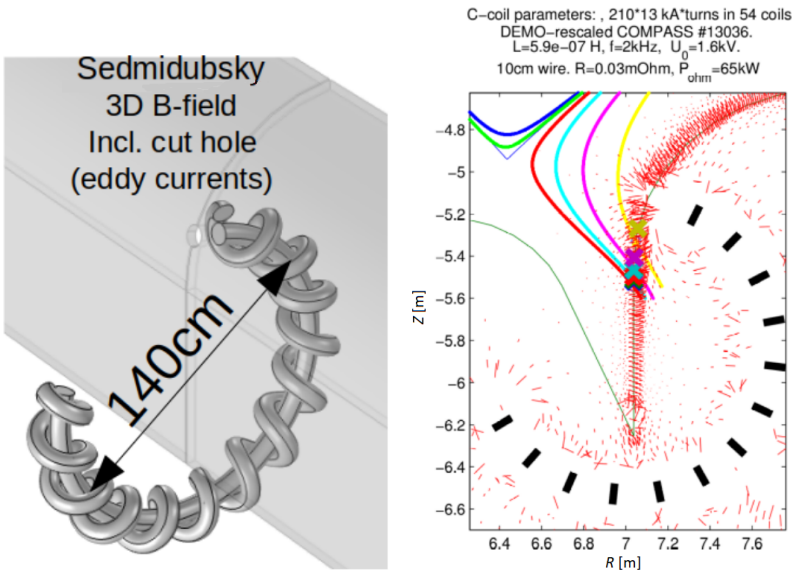

a) b)

Figure 9: a) *3D display of one of the* 54×2 *coils, which starts from behind the divertor PFCs and ends in the radial middle of the divertor region. A poloidal cut is made in the PFC support structure, which represent the non-conductive contact of two adjacent EU DEMO divertor cassettes. At the mouth of the coil, the cut is widened to a circular hole.* b) *The result of the MATLAB code following the magnetic field lines in the tokamak magnetic configuration summed with the field from the sweeping coil, shown in poloidal cross-section. Obtained and modified from [13].*

In Figure 9b we can see the resulting shape of open (not closing within the tokamak vessel) magnetic field lines. In the approximation of strong magnetic fields ($r_{\mathrm{L}} \ll$ the

typical size of any divertor component) and low collisional plasma ($\frac{1}{ion\ collisional\ frequency} \ll$ *divertor connection length* $\cdot$ *ion parallel velocity*), the field lines represent plasma streamlines. It is the result of a MATLAB Field-line Tracking code [37], which followed the direction of the magnetic field in cylindrical geometry (sufficient approximation of the reactor torus). The coil magnetic field was calculated in COMSOL Multiphysics software and added to the re-scaled magnetic configuration from COMPASS tokamak to EU DEMO dimensions.

It is obvious that this system of 2x54 copper coils (each weighs 900 kg) occupies a substantial part of the divertor cassette. Their use is therefore more advantageous within a larger reactor. It is important to keep in mind that a separate circuit with high-voltage capacitor banks is also a significant financial and space issue, at least the capacitors and switches can be located far enough from the reactor.

2.4.3 Performance

Another 2D MATLAB Heat Conduction code [13] used scaled data from an infra-red camera from JET tokamak. The camera recorded the time evolution of the tungsten tile surface temperature at the *strike-point* during one of the world-largest ELMs. The obtained profile of the incident heat flux was scaled in amplitude, space and time [13]. Figure 10 shows the result of the simulation, where 4× lower tile surface temperature compared to the situation without fast sweeping is obtained.

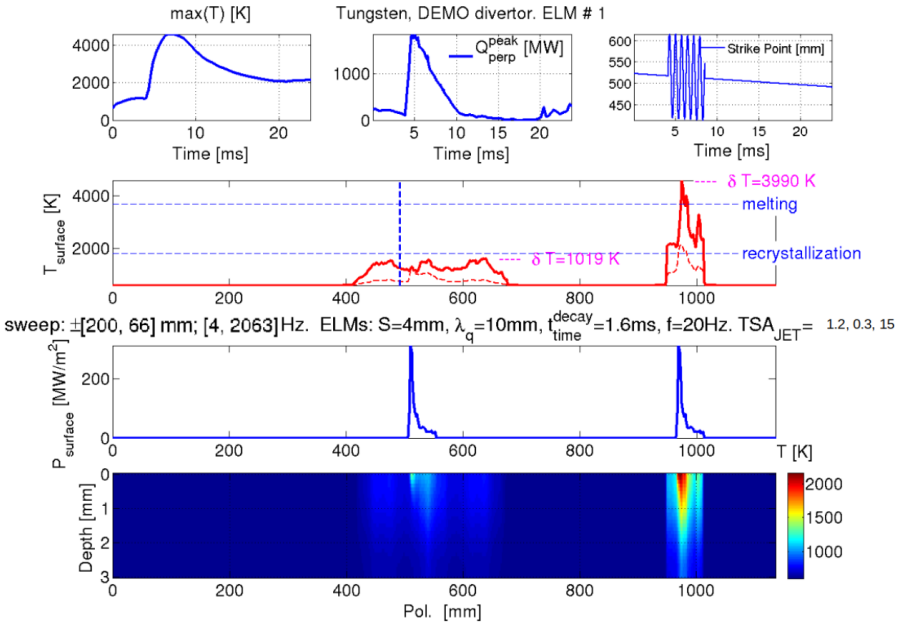

Figure 10: *Results from the heat conduction simulation of tungsten divertor target after one ELM. The ELM divertor surface temperature sweeping suppression factor* $F_{STS} = \frac{3990\ K}{1019\ K} = 4$ *when strike-point is swept with* 66 *mm amplitude and* 2063 *Hz frequency. The simulation includes also the slow strike-point sweeping of* 200 *mm amplitude at* 4 *Hz. Obtained from [13].*

According to version from [28], the coil would have to sustain 2 kHz regular $I \times B_{\text{tor}}$ huge force of 800 kN, thus any rigid attachment would yield vibrational fatigue. Instead, leaving it freely rotate along horizontal axis (as shown in Figure 11), the force acting on a 600 kg heavy coil inertia results in only 0.1 mm vertical displacement for each ELM-sweeping 2 ms long event. Since odd/even ELMs start with positively/negatively charged capacitor, respectively, those rotational skips alternate direction and thus keep the coil displacement within 0.1 mm range. In the case of a newer sweeping system, proposed in this work, we consider its parameters to be very similar, thus also neglecting the vibrations.

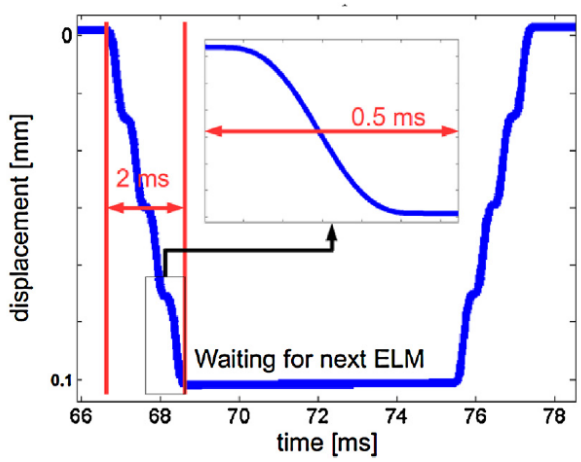

Figure 11: *Expected vertical sweeping coil displacement during two subsequent ELMs. Each ELM contains* 4 *sweeps. Obtained from [28].*

To ensure the same conditions for each subsequent ELM and prevent the overheating of the cooling water, it is necessary to combine both fast and slow sweeping. While the fast sweeping suppresses thermal shock during one ELM, the slow sweeping must move the strike-point to a position unaffected by the ELM. However, this system does not fully include eddy currents, does not address the interaction of the sweeping magnetic field (< 1 T, ~ 2 kHz) with the surroundings, and does not contain the correct EU DEMO magnetic field configuration.

2.4.4 RLC circuit

It is considered to connect each of the coils to a separate undriven series RLC circuit. The RLC circuit represents the connection of three electrical components: a resistor with an electrical resistance R, an inductor (coil) with an inductance L and a capacitor with a capacitance C. When talking about a *series* RLC circuit, the components are connected one after another. And when talking about an *undriven* RLC circuit, then the circuit is not connected to an external voltage source (external voltage source can only charge the capacitor, as seen in Figure 12b). If the capacitor is charged in such circuit and

then the circuit is switched, energy will begin to flow from the capacitor to the magnetic field around the inductor and back. This exchange will be harmonic with a frequency $f_0 = \frac{1}{2\pi\sqrt{LC}}$, called the resonant frequency.

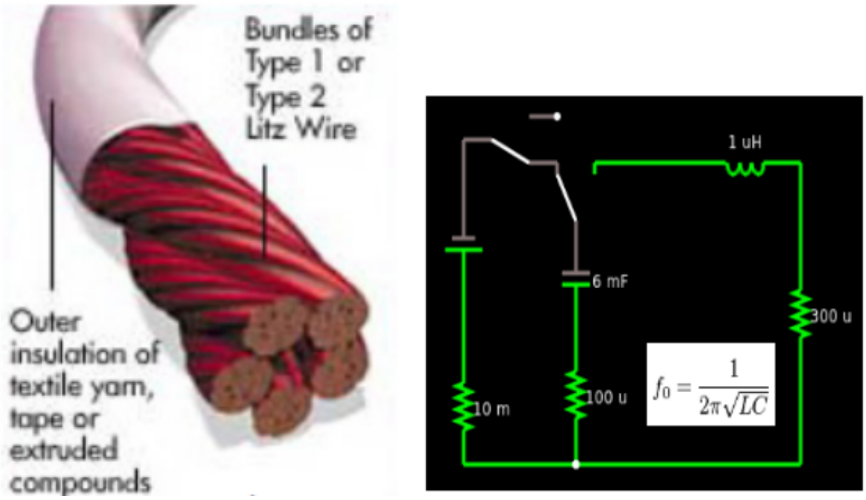

a) b)

Figure 12: a) *An example of wiring with Litz wire technology, which forces a high-frequency current to flow evenly across the cable cross-section to avoid large losses.* b) *Schematic of considered undriven series RLC circuit. Obtained and modified from [13].*

In [13] 2×54 of such circuits are described having capacity $C = 6$ mF given purely by capacitors charged with DC voltage of $V = 3.2$ kV and inductance $L = 1.4$ μH, which represents only the field induced by sweeping coil. It is assumed that the components are connected (and the coil constructed) using so-called Litz wires (see Figure 12a), which negate increasing losses in AC lines when compared to DC. This gives the circuit less resistance $R = 28$ μΩ, but the total losses of all circuits (taking into account the duty cycle given by the frequency of ELMs) are still $P_{\text{ohmic}} = 3.5$ MW when the amplitude of AC current is $I = 210$ kA. The losses in orders of MW and the price and size of the system itself already raise the question of whether this method is applicable in practice when reducing surface temperatures by factor of $F_{\text{STS}} = 4$.

2.5 Alternating Magnetic Conductor

However, the mentioned concepts of fast sweeping suffer from the presence of induced eddy currents, which cause a significant interaction of the coils with the tokamak structure and the surrounding systems. This greatly impairs the penetration of the magnetic field through the protective heat shield of the vessel and thus unnecessarily increases the required power of the sweeping system. The coils themselves and their supply cables also take up a lot of volume in the area behind the divertor, and it is therefore desirable to move them to more distant areas, which again increases the demands on the magnetic field. Therefore,

between 2020 and 2021, a number of proof-of-principle experiments were conducted, which aimed to test a new concept of passive focusing of alternating magnetic field using the so-called Alternating Magnetic Conductor (AMC) [38].

AMC is a conductive tube of any shape through which a cut is made along its axis. The source of the alternating magnetic field (a coil) of frequency f is located at the selected position inside the tube. We orient the coil so that its axis lies on axis of the tube, see Figure 13b. The coil excites a magnetic field that cannot pass through the tube's conductive material of conductivity σ and magnetic permeability μ due to the induction of eddy currents negating the local original magnetic field. The damped magnetic field thus drops to 1/e of its original amplitude in the thickness of

$$\delta = 1/\sqrt{\pi f \sigma \mu} \quad [39] \qquad \text{(for copper and 1 kHz: } \delta = 2.1 \text{ mm)} \tag{31}$$

For AMC to function fully, its thickness must be greater than δ.

The mentioned cut of the tube (AMC) is very important. If the tube had no cut, eddy currents would create the exact opposite magnetic field, which would negate the entire original field. Such result is an implication of the eddy currents behavior trying to prevent the passage of a component of the magnetic field which is perpendicular to the surface of the material. This is also the case with the cut tube, but the eddy currents must now take on a different configuration, which in principle does not allow the magnetic induction lines to go anywhere other than along the tube, see Figure 13b. And since the density of the magnetic field lines can be identified as the magnetic flux density Φ ($\Phi = B \cdot S$ for a constant magnitude B of the magnetic field parallel to the surface with a total area S), it is clear that with a constant density of the magnetic field lines along the axis of the tube, magnitude of the magnetic field does not change either.

At first sight, AMC could be mistaken for a waveguide, but theory and practice work completely differently. The propagation of a wave in the waveguide is given by differential equations with boundary conditions at interface of the waveguide walls and the inside of the waveguide. The possible results are different wave modes with frequencies given by the geometry and material of the waveguide. AMC, on the other hand, has a clear frequency monotone increasing solution. The main difference compared to the waveguide, however, lies in the longitudinal cut of AMC, which, in turn, would completely destroy the waveguide. AMC must also be completely conductive, while waveguide can be also constructed of dielectrics.

Furthermore, AMC could be mistaken for a magnetic shielding made of ferromagnetic material ($\mu_\mathrm{r} \gg 1$), but the difference is also obvious. The AMC cannot shield the stationary field because used copper has the relative magnetic permeability $\mu_\mathrm{r} \doteq 1$. This gives AMC an interesting advantage over shields made of ferromagnetic materials, because in the tokamak the strongest magnetic field is stationary $\frac{\partial B_\mathrm{toroidal}}{\partial t} = 0$, so it does not exert any

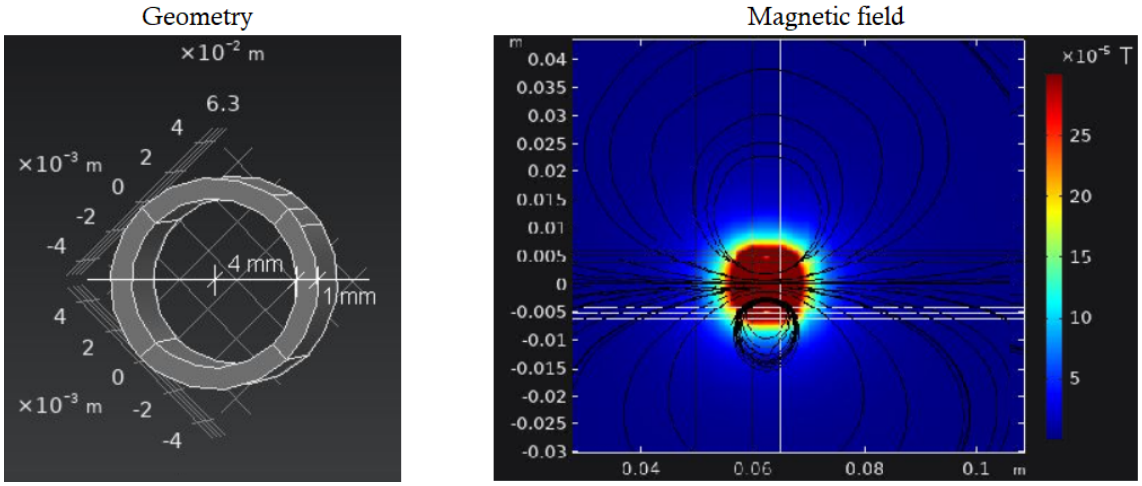

a)

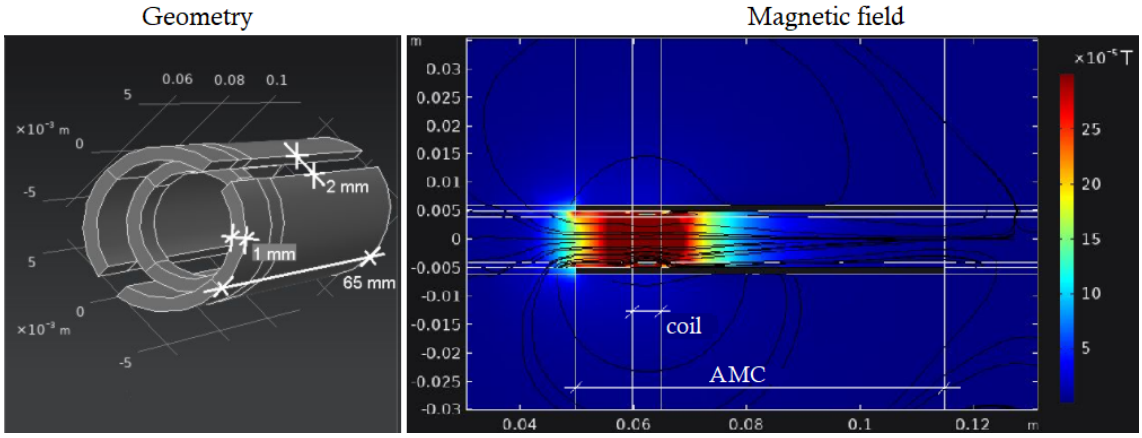

b)

Figure 13: *AMC operating principle. Figure* a) *shows only the coil and in section its magnetic field including the field lines. Figure* b) *shows the resulting magnetic field when using AMC.*

force on AMC.

2.5.1 Experiments

The main goal of the experiments was to confirm/refute the original assumptions, find suitable configurations and find out some scaling dependencies. We were later able to scale the obtained results with the help of numerical simulations, the use of which to find the basic principles would be unreliable and unnecessarily laborious.

The most important thing for us was the result of an experiment, where a copper plate with a cut was inserted in front of the excitation coil. In the case of placing the excitation coil in AMC, which was subsequently non-conductively pressed to the plate, there was a significant increase ($> 10^1\times$) of the magnetic field behind the plate, compared to the case without AMC. This experiment confirmed the basic idea of AMC in a topology similar to the placement of sweeping coils on the DEMO divertor.

A more practical experiment was to find the best AMC possible. The excitation coil was inserted into different AMCs at different positions from the ends of AMC, measuring the magnetic field at the mouth of AMC. Figure 14 shows a comparison for 9 different AMCs. The best AMC is the one that shows the smallest possible change in the magnetic field at the mouth of AMC when the position of the excitation coil changes. This definition is best met by AMC consisting of a conductive aluminum foil layer and an insulating layer of paper, which are applied to each other and spirally wound into a tube shape.

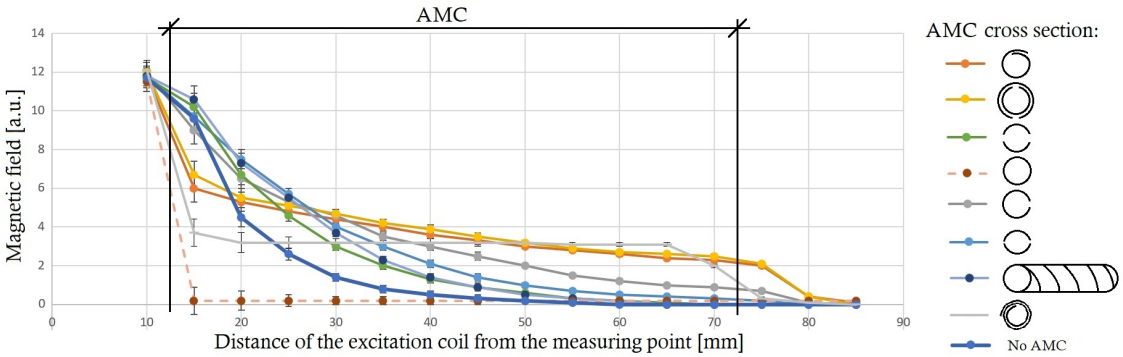

Figure 14: *Measured magnetic field at the mouth of different types of AMCs for changing the position of the excitation coil inside AMCs.*

It can also be seen that the better AMC, the lower the magnetic field values can be measured at closer distances of the excitation coil to the mouth of AMC. In other words, for a given AMC, there is a certain distance of the excitation coil from the mouth of AMC for which AMC begins to be useful. AMC seems to be somehow keeping the original magnetic energy, only changing the shape of the magnetic field, further research is required in order to better understand.

2.5.2 Simulations

Simulation software COMSOL Multiphysics was used to scale the experiments. An arrangement similar to that in the experiments in Figure 14 was modeled in it. By comparison with the results from the simulations, see Figure 15, it was found that the results do not agree for "too good" AMC (according to the quality definition in Section 2.5.1). This led to the decision that only AMC type consisting of a tube with one longitudinal cut would continue to be considered in the simulations.

The following simulations were converted to geometry from [13] approximately corresponding to the current geometry of the EU DEMO divertor. AMC was placed around the sweeping coil in form of a conductive cylinder with a cut. Comparison of the simulations revealed up to 3× larger magnetic field around the *X-point* induced by the sweeping coil when using AMC [38].

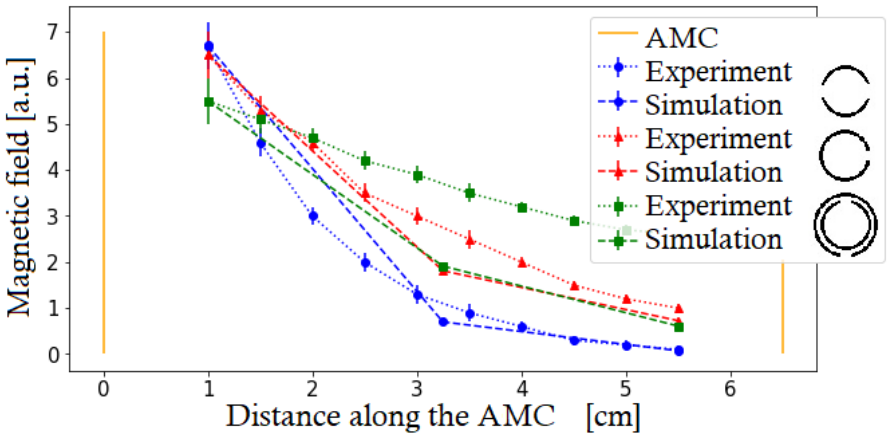

Figure 15: *Comparison of simulation with experiment. The coil is inserted into AMC at various positions, measuring the magnetic field at the mouth of AMC.*

3 Magnetic field simulations

COMSOL Multiphysics software (used builds 5.2, 5.6 and 6.0) was used to simulate magnetic field of the sweeping coils. It is a cross-platform finite element analysis, solver and multiphysics simulation software. We chose it because of its widespread support and very user-friendly environment, which does not degrade its accuracy. On the contrary, COMSOL has thus become a very simple and accurate tool that allows one to quickly modify a simulation during research. Only one of its many modules, the AC/DC Module, was sufficient for this work. This module offers several solvers for a wide variety of electromagnetism physics.

The interface we have used the most is called *Magnetic Fields*. It is used to compute magnetic field and induced current distributions in and around coils, conductors, and magnets. It solves Maxwell's equations, which are formulated using the magnetic vector potential $\mathbf{A}$ and, optionally for coils, the scalar electric potential ϕ as the dependent variables.

$$\mathbf{B} = \nabla \times \mathbf{A}, \qquad \mathbf{E} = -\nabla\phi - \frac{\partial \mathbf{A}}{\partial t} \tag{32}$$

To correctly distinguish the interaction of different materials in a wide range of electromagnetic frequencies, the module offers several physical conditions and approaches, which we will now discuss.

3.1 Simulation settings

Given the nature of the simulations, i.e. magnetic field around the harmonically swept coil at frequency $f = \frac{\omega}{2\pi}$, it was logical to choose the so-called *Frequency Domain Study* (or called the *Fourier Domain*). The time-dependent variables ($\mathbf{A}(t)$, $\phi(t)$, $\mathbf{B}(t)$, $\mathbf{E}(t)$, ...)

thus obtain a prescription of form

$$V_i(t) = V_i \cdot \exp^{i(\omega t + \varphi_{V_i})}, \qquad s(t) = s \cdot \exp^{i(\omega t + \varphi_s)}, \tag{33}$$

where V_i is the amplitude of the i-th component ($i \in \{1; 2; 3\}$) of $V_i(t)$ of any vector variable $\mathbf{V}(t)$ and s is the amplitude of any scalar variable $s(t)$. φ_{V_i} and φ_s then indicate the phase shift of the individual variables. This makes it possible to completely exclude the time dependency of variables from the equations, and the algorithm then uses one of the iterative solvers, which only needs to be converged once, so the simulation can be many times faster. As a result, only a real part of the complex solution is sufficient and can be written in the harmonic form

$$V_i(t) = V_i \cdot \cos(2\pi f \cdot t + \varphi_{V_i}), \qquad s(t) = s \cdot \cos(2\pi f \cdot t + \varphi_s) \tag{34}$$

By choosing the *Magnetic Fields* interface, we get a set of three elementary nodes that form the necessary basis of physical equations.

- *Ampère's Law* node adds the Ampère's law for the magnetic field and provides an interface for defining the constitutive relation and its associated properties as well as electric properties.

- *Magnetic Insulation* node adds a boundary condition that sets the tangential components of the magnetic potential to zero at the boundary

$$\mathbf{n} \times \mathbf{A} = 0 \tag{35}$$

- *Initial Values* node adds an initial value for the magnetic vector potential for a nonlinear solver. We choose the default value of

$$\mathbf{A} = 0 \tag{36}$$

The modeling of the coil itself was simplified compared to previous work in Section 2.4, where the coil had a real 3D structure of a curved solenoid. Now the coil was represented by a hollow cylinder modeled using an internal node known as *Coil*. The *Coil* node was set to *Homogenized Multi-turn*, which models a bundle of wires tightly wound together. *Circular* coil geometry subnode was added in order to simulate the sweeping coil.

Because EU DEMO cassette size ratio is approximately 3:1 (radial:toroidal), there is a significant interaction of toroidally adjacent coils. We therefore introduced *Periodic Boundary Conditions* node into the model with the so-called standard periodicity settings

for which

$$\mathbf{A}(x_1) = \mathbf{A}(x_2), \tag{37}$$

where x_i represent the coordinates of periodic boundaries.

BiCGStab Iterative Solver was used for solving the resulting linear system of equations. This solver uses the biconjugate gradient stabilized iterative method, which we assumed as the most stable method throughout the variety of simulations.

We had to adjust mesh of the simulated geometry several times for the solver to find a solution. It is a problem of simulating the cassette of a very large size (few meters) relative to millimeter gaps in AMC. Few details of resulting mesh can be seen in Figure 16.

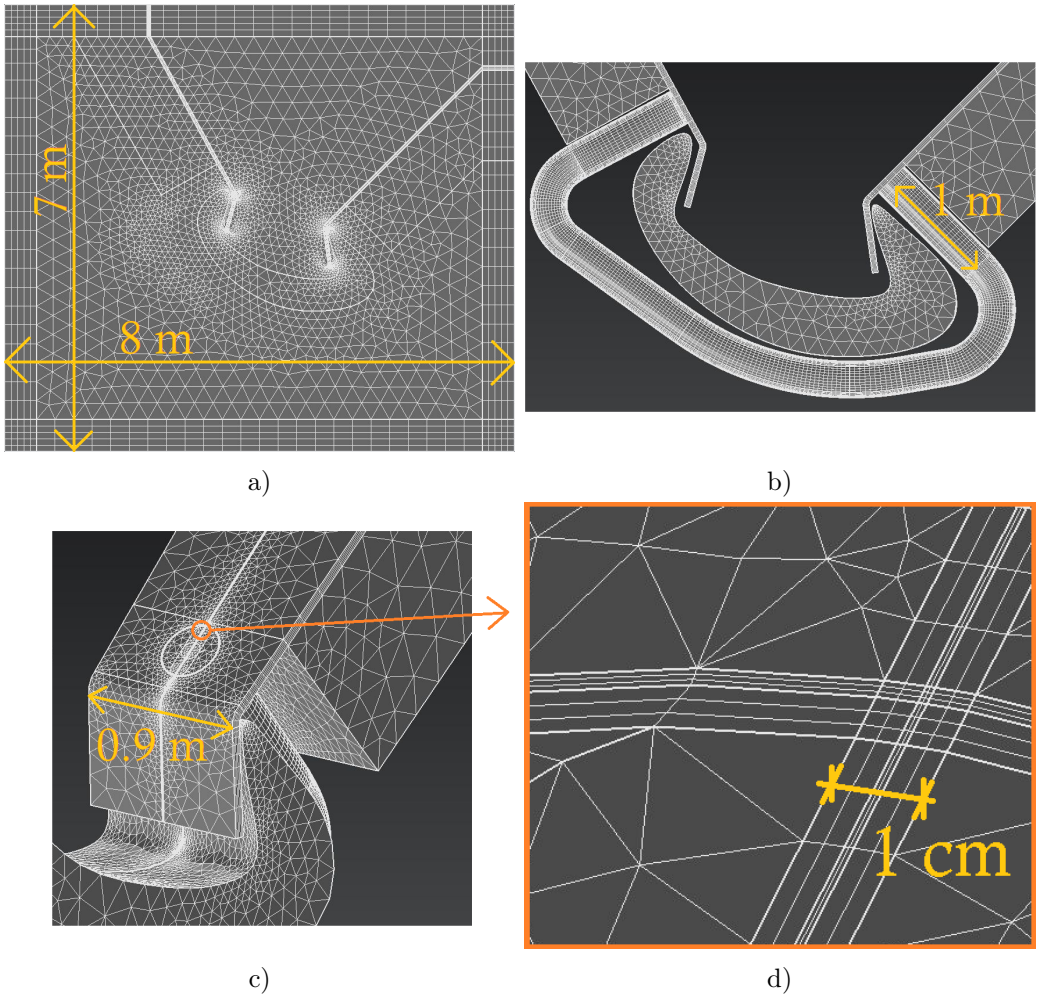

Figure 16: a) *View on resulting mesh showing the difference in sizes of mesh elements in various areas.* b) *Mesh of vacuum space is removed in order to see meshed AMC.* c) *View on PFC mesh and* d) *shows its detail where the mesh of AMC crosses the mesh of PFC. Total mesh consist of* 10^6 *domain elements* (10^7 *degrees of freedom) which results in total computation time of* 4 *CPU hours (core frequency of* 2.9 *GHz) per simulation while occupying up to* 100 *GB of RAM on Soroban computational cluster located on IPP of the CAS.*

3.2 EU DEMO configuration

We started with a 3D model of the divertor cooling system in ITER-like divertor cassette from 2016, see Figure 17. The cassette has been greatly simplified into a homogeneous structure copying the edges of the model to save computational time (limited by the used computer cluster node). One convergence should not take more than ∼an hour, because the geometry itself and various aspects of the simulation have changed countless times during the research. Due to the need to simulate magnetic field even outside the cassette, around blanket, the rest of the geometry including PFCs was obtained from the contours from the tokamak poloidal cross-sections [40].

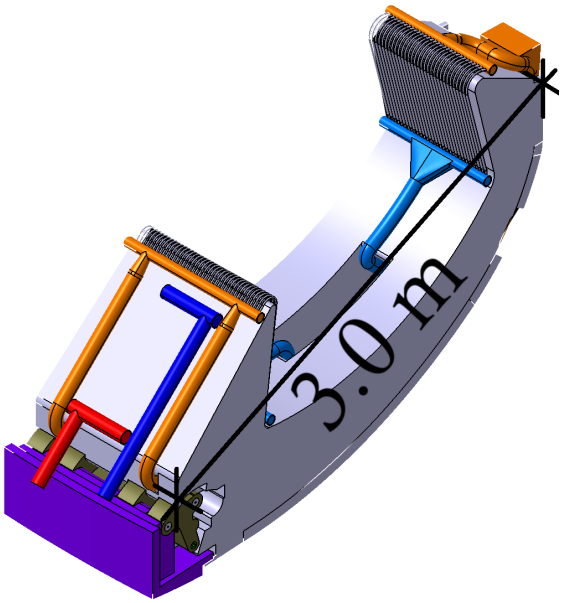

Figure 17: *The original model of the divertor cassette from 2016, which was resized for EU DEMO to match CREATE DEMO magnetic equlibria [37].*

The coils themselves have been placed outside the divertor cassette, which greatly facilitates their implementation compared to previous work. The weight of one coil is ∼ 2 t and any intervention in the complicated cooling network in the cassette is not preferred from an engineering point of view. This placement also allowed us to implement AMC more arbitrarily. AMC was made of 3 mm thick copper sheet (skin-depth $\delta_{1.2\mathrm{kHz}} = 2.3$ mm), its surface was 5 mm away from the edges of the coil and AMC connected every two coils in one toroidal segment. The aim of the interconnection was to improve the penetration of the magnetic field through the conductive PFC structure and to prevent the interaction of 1 kHz magnetic field with surroundings.

Eventually, the entire geometry was cut into the shape of two adjacent halves of two adjacent toroidal segments, see Figure 18. It can be seen that the coil system is thus toroidally offset from the cassette arrangement by half a cassette. The cut between the individual cassettes is 1 cm wide; with a narrower cut, penetration of the magnetic field

is suppressed. The radially converging edges of the simulated geometry are replaced by a periodic boundary condition, so the resulting simulation corresponds to the actual toroidal geometry.

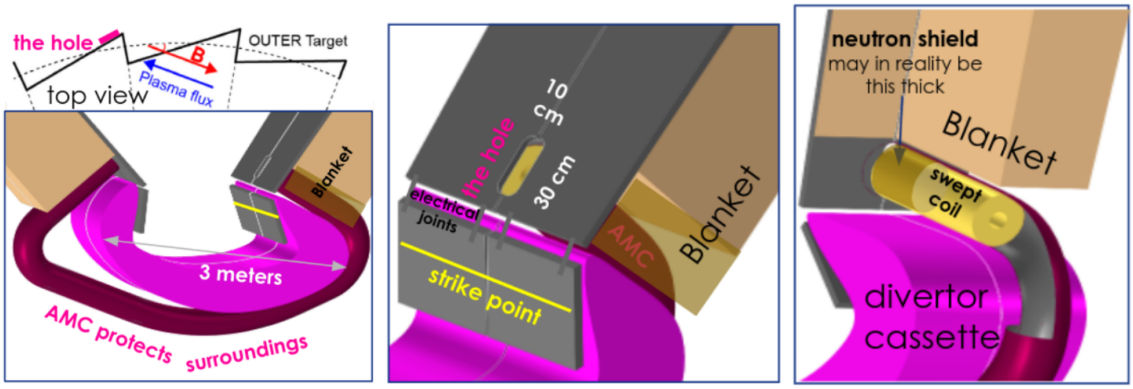

a) b) c)

Figure 18: a) *Resulting geometry of simulations. Dark red color represents AMC made from copper, yellow colored are the copper sweeping coils, gray is the nearest PFC support made from EUROFER 97 as is the pink colored divertor cassette and brown colored blanket* b) *Detail for a suitable cutout in PFC, which is located outside a possible position of the strike-point and is in the magnetic shadow behind the adjacent inclined PFC (as seen on top of* a)*).* c) *Cut through AMC showing the coil location.*

3.3 Optimization

Due to the still evolving design of EU DEMO, there is not much information about the construction of the tokamak in the vicinity of the divertor, so we did not focus so much on optimizing the mouth and rotation of the coils relative to the *strike-point*, but more on which parts should be left separate and how far (divertor consist of 54 replaceable cassettes) and which would be appropriate to conductively interconnect. So we placed the coils perpendicular to PFC structure and close enough to the *strike-point* to avoid overlap with the divertor cassettes.

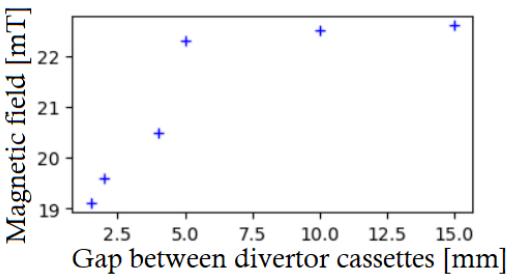

Figure 19: *Dependence of magnetic field strength (∼ 10 cm away from outer strike-point) on the gap width between adjacent divertor cassettes. All points are calculated for frequency* $f = 1.6$ *kHz, gap width in AMC* 1 *mm and* 10 *kA in* 100 *turns per coil.*

Because the tokamak magnetic confinement (or any other toroidal device) is in principle worse on LFS, the thermal load is proportionally worse on outer *strike-point*. Therefore, we continued to implement the system only for the outer *strike-point*, because for inner *strike-point* conditions are expected to be automatically met.

More difficult was to choose a suitable gap thickness between the toroidal segments (gap in AMC is fixed). We did not know the possible width of the gap, but as the simulations showed, the larger the width, the more the magnetic field passes through, see Figure 19. To maintain the toroidal integrity of PFC, we fixed the width to 1 cm, which is still less than the toroidal inter-cassette gap on ITER 20 ± 5 mm [41]. So if EU DEMO inter-cassette gap will be larger, the sweeping efficiency will also improve.

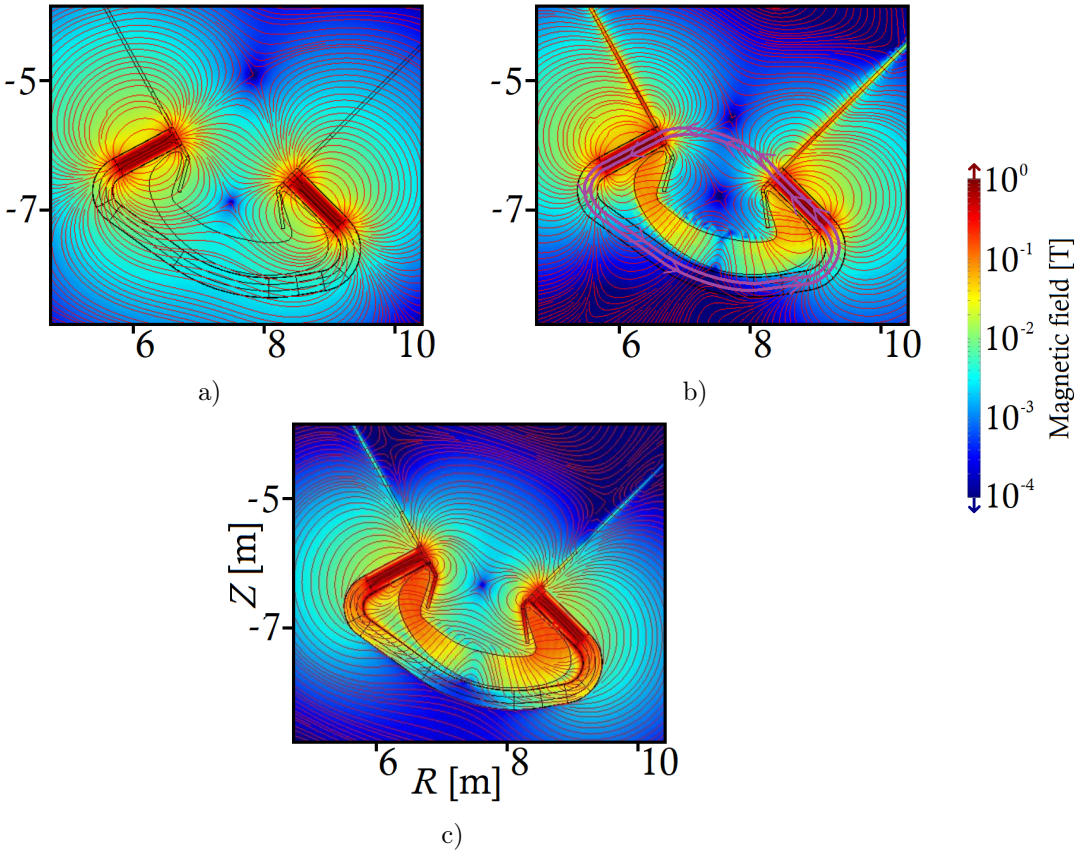

Figure 20: a) *Cross-section (in the middle of the toroidal gap) of the resulting magnetic field (in its amplitude), where only copper coils in a vacuum are considered (the contours of tokamak geometry indicate only the location of the coils). The red lines follow the direction of magnetic field so that their density is constant throughout the image (unlike magnetic field lines).* b) *The cassette and a* 5 *cm thick PFC support structure from EUROFER 97 are added. Thicker purple lines indicate the idea of the best possible shape of field lines, which we try to achieve via AMC.* c) *Copper AMC was added (guided from coil to coil around the cassette). A return to a stronger magnetic field in the plasma region is evident. The blanket modules are missing here, but they do not influence the magnetic field inside the divertor region [37]. All 3 options are simulated for* $f = 1.6$ kHz.

Increasing field penetration through a larger gap in PFCs makes sense, but on the other

hand, our goal was (in the idea of magnetic field lines as streamlines of abstract fluid) to use AMC to enclose magnetic field lines in some kind of circuit closing in part in AMC, passing only through the additional hole in PFCs at the mouth of the coils (not through the inter-cassette gap) and more passing near the *X-point*, see Figure 20b. The resulting constant magnetic field line density would lead to a stronger magnetic field at the *X-point* position, where the original tokamak poloidal field is $B_{\mathrm{pol}} = 0$. There, in principle, would be the greatest change in the magnetic field topology $\lim_{B_{\mathrm{pol}}^{\mathrm{original}} \to 0} \frac{B_{\mathrm{pol}}^{\mathrm{sweeping}}}{B_{\mathrm{pol}}^{\mathrm{original}}} \to \infty$, and since the change in the trajectory of the particles accumulates along its path, we would get the best sweeping efficiency. However, as mentioned in Section 2.5.2, AMC used does not achieve the desired qualities and the result from Field-line Tracking [37] shows $\sim 2\times$ lower efficiency when using thinner inter-cassette gaps (such result therefore corresponds to Figure 19).

As the main difference between Figure 20b and Figure 20c is the addition of AMC we can present you the efficiency of AMC. Without AMC, the Field-line Tracking simulations [37] shown $4\times$ lower sweeping amplitude (F_{STS} decreased by 30%) when the same ohmic losses were accounted for.

Another parameter is a gap in AMC, but it is clear here that we want to achieve the smallest possible gap. Unfortunately, even with multiple AMC layers, we will not achieve the desired AMC quality, see Section 2.5.2. There is a certain saturation of computational capabilities, where due to the narrower gap, the simulation is no longer able to monitor the growing quality of AMC (even when mesh is more and more finer), see Figure 21. We therefore fixed the gap thickness in AMC to 1 mm (but we know from experiments that a better AMC could actually be made and therefore more efficient sweeping system).

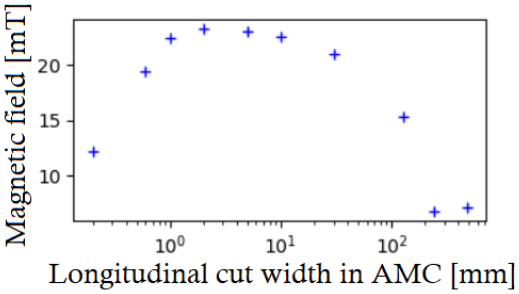

Figure 21: *Dependence of magnetic field strength ($\sim$ 10 cm away from outer strike-point) on the AMC longitudinal cut width. All points are calculated for frequency $f = 1.6$ kHz, gap in divertor 1 cm and 10 kA in 100 turns per coil.*

We then followed up on an attempt to improve the enclosure of the magnetic field lines from both coils, as in Figure 20b. Figure 22 shows the results of several possible ways of conductive interconnection of divertor cassettes, which show that the strongest magnetic field is still obtained in the case where no additional interconnection is made (confirmed by Field-line Tracking simulation). This is good in principle, because even

at ITER, PFCs themselves are segmented into monoblocks with dimensions 28 × 12 × 28 mm (Tor×Pol×Rad) [41], not only for thermal expansion but also to prevent current induction during distributions. The reduction of the magnetic field at the *X-point*, despite the prevention of return of the divertor-hole-passed field lines other than through the second coil, is explained by the fact that more field lines are enclosed in AMC volume itself (e.g. they are more compressed in close proximity to the sweeping coil)

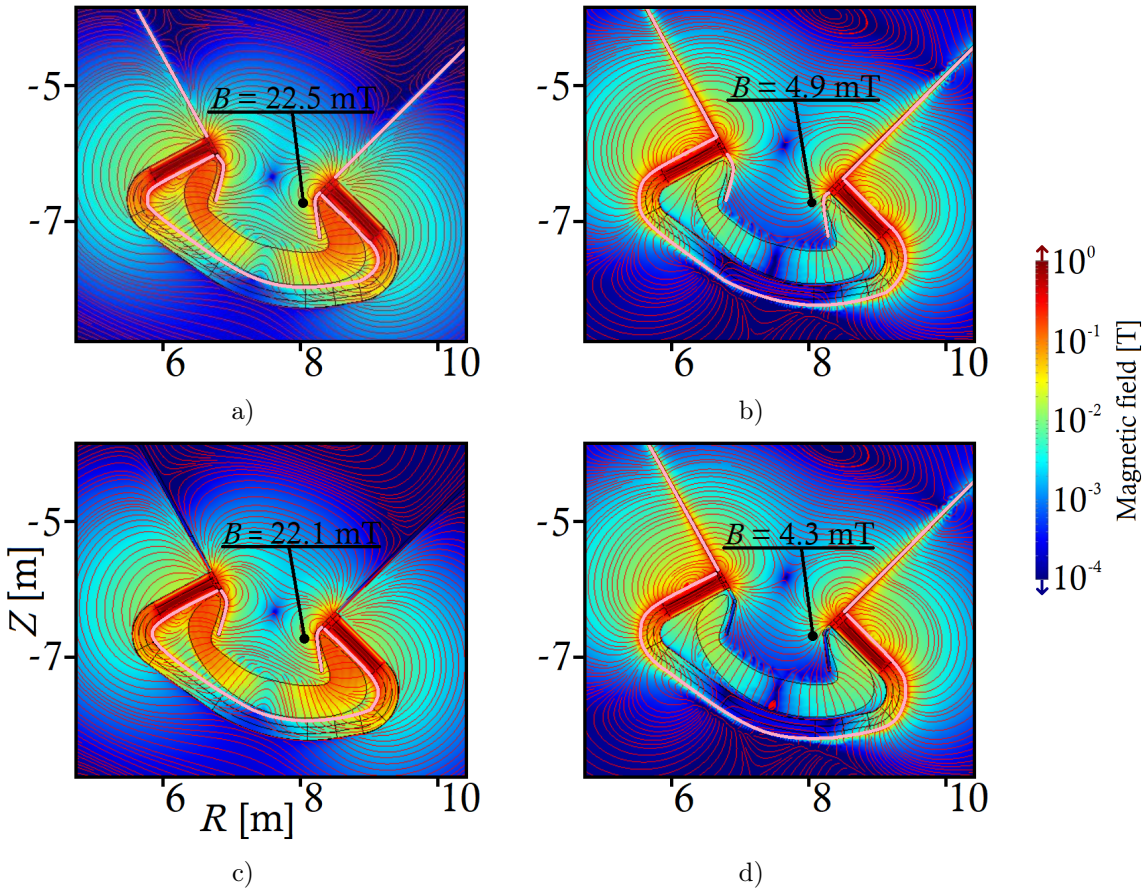

Figure 22: *Poloidal cross-section (in the middle of the toroidal gap) of the simulated magnetic field (in amplitude) for different arrangement of gaps between toroidal segments in PFC and AMC. The gaps corresponding to each configuration are highlighted by a pink line. The simulations also include a gap in the cassette in which the view is located. The gaps have a possible thickness in PFC of* 1 *cm and in AMC of* 1 *mm. The blanket modules are missing here, but they do not influence the magnetic field inside the divertor region [37].*

Because we see in Figure 20c that the dominant magnetic field strength reaches only to about half of the total length of simulated AMC (given by AMC quality), halving AMC can save space around the divertor cassette at the cost of a small reduction in AMC quality. In Figure 23 we can see a comparison of the resulting fields, where near the strike-point in the case a) we get almost the same value of the magnetic field $B^{\mathrm{AMC}}_{\mathrm{long}} = 22.5$ mT as in the case b) $B^{\mathrm{AMC}}_{\mathrm{short}} = 22.2$ mT. However, we must keep in mind that such a volume saving only works in the case of currently used AMC, which is not able to fully extend the magnetic

field through its volume (in Section 2.5.1 we see that a much better AMC can be made).

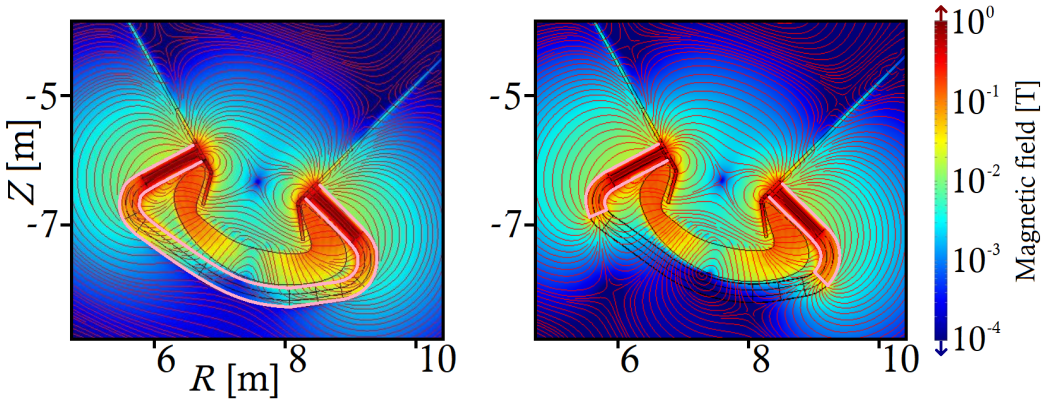

a) b)

Figure 23: *Difference between* a) *fully interconnected coils via AMC and* b) *AMC shortened by* $\approx 50\%$ *and without any difference inside the divertor region. The shortening is sketched around the AMC boundary with a pink line.*

3.4 Frequency dependence

In previous works (see Section 2.4), the dependence of results on frequency was caused only by the penetration depth of eddy currents. Due to the used tungsten structure with a thickness of 10 cm, it was so far negligible, so that the frequency dependence has not yet been described for the selected geometry and frequencies ($\delta^{\mathrm{W}}_{1\mathrm{kHz}} = 3.8$ mm). But in this work, we will see that there are even two other important factors that cause frequency dependence.

Due to the higher frequencies required to apply the fast sweeping principle (ELM time scale $\tau_{\mathrm{ELM}} = 3$ ms $\gg$ sweep period $1/f$), we also neglected the effect of the variable penetration depth into the material. However, because eddy currents can be viewed as a secondary electrical circuit connected to the main sweeping circuit via electromagnetic induction (such as a transformer), a frequency-dependent phase shift of the eddy currents I_{e} relative to the primary current I_{s} can also occur. Such a phase shift can manifest itself in two ways:

1. Because both currents $I_{\mathrm{e,s}}$ create harmonic oscillations of magnetic fields $\mathbf{B}_{\mathrm{e,s}}$ their sum $\mathbf{B}^{\mathrm{sweeping}}$ will also be a harmonic function. $\mathbf{B}^{\mathrm{sweeping}}$ amplitude (sweeping efficiency) depends on the relative phase shift of $\mathbf{B}_{\mathrm{e}}$ and $\mathbf{B}_{\mathrm{s}}$.

2. Since we consider Figure 20b to be intuitively the best magnetic arrangement (or also to try to get as many magnetic field lines as possible in the direction perpendicular to the original poloidal field: $\max(\frac{B^{\mathrm{sweeping}}_{\mathrm{pol}}}{B^{\mathrm{original}}_{\mathrm{pol}}} \cdot \frac{\mathbf{B}^{\mathrm{sweeping}} \times \mathbf{B}^{\mathrm{original}}}{B^{\mathrm{sweeping}} B^{\mathrm{original}}})$, we could also quickly (no need to run Field-line Tracking simulation) guess the sweeping efficiency only from cross-sections of magnetic field. And because the resulting field $\mathbf{B}^{\mathrm{sweeping}}$ is the

sum of $\mathbf{B}_e + \mathbf{B}_s$, the phase shift of field $\mathbf{B}_e$ is visible in the poloidal cross-section of $\mathbf{B}^{\text{sweeping}}$.

3.4.1 Ion fly-time

The second factor of frequency dependence is a flight time of Deuterium ions along the sweeping coils. Because this phenomenon is not part of the simulations in COMSOL, but is part of the Field-line Tracking simulations, only the principle and results are described here, as in [37].

According to [42], electron temperature at divertor during ELM $T_{e,ELM}^{divertor} \approx 0.8 \cdot T_e^{pedestal}$, where $T_e^{pedestal} \approx 5$ keV is electron temperature which diffuses from the plasma outside of LCFS. Therefore, the fly-time of Deuterons with the corresponding speed $c_s = \sqrt{2T_i e/m_D} = 700$ km/s through the region of only one coil is $\frac{2\pi R}{Nc_s} = 1.2$ µs. Each ion passes through $\sim 50 - 100$ coils. During 100 µs the sweeping current with frequency $f \approx 1$ kHz vary significantly. Extremely slow ions even switch direction of the coil's perturbation during their flight. The ions at the velocity distribution tail, carrying most of the ELM energy, fly faster than c_s and thus are insensitive to this problem. For $T_{i,ELM}^{divertor} \geq 5$ keV and $f < 4$ kHz the 3D Field-line Tracking simulation yields $\leq 20\%$ weaker *strike-point* sweeping amplitude.

In COMSOL, we simulated the behavior for several frequencies. Calculated magnetic fields were passed into Field-Line Tracking simulations the resulting sweep amplitude $\lambda_{sweep}(f)$ can be seen in Figure 24. Therefore, a small correction to λ_{sweep} will be assumed later in the circuit analysis.

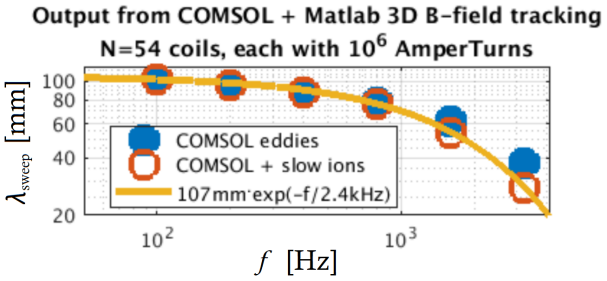

Figure 24: *The overall desired strike point shift λ_{sweep} for 16 kA×63 turns×54 coils. Eddy currents in the divertor structure and AMC generate (undesirably) a decreasing frequency dependence. Similarly, the effect of slowly flying ions further weakly decreases the strike point shift amplitude.*

4 Sweeping circuit

As important as the sweeping magnetic field acting on the *strike-point* is an analysis of the circuit that generates the field. As in previous works, we will stick to the reso-

nant frequency of RLC circuit, see Section 2.4.4. The main difference is an analysis of interdependent circuit parameters, the search for real components in current market and consideration of two ways to connect the RLC circuit. Thanks to this, we were able to find the most optimal solution with the greatest possible efficiency against losses, which is also achievable with current technology.

4.1 Analysis

The idea was to represent as many important quantities as possible, especially ohmic losses $E_{\Omega}^{\mathrm{ELM}}$ per ELM and F_{STS}, on some chosen parameter. We chose the number of turns per coil N_{turns}. In calculations, we keep the sweeping amplitude λ_{sweep} constant (we assume $\lambda_{\mathrm{sweep}} \sim N_{\mathrm{turns}} \cdot I_{\mathrm{s}}$) and consider the total length of connection cables $d_{\mathrm{cable}} = 100$ m (from the capacitor to the coil). We also keep constant the coil volume $V_{\mathrm{coil}} = 0.07$ m^3 and mass $M_{\mathrm{coil}} = 2$ t.

For every N_{turns} we start by calculating total circuit inductance $L = L_{\mathrm{coil}} + L_{\mathrm{cable}} + L_{\mathrm{CES}}$, which consists of several components connected in series:

- The main part of L is, of course, the strong field generated from the sweeping coil itself, which is calculated using the total energy of magnetic field in the simulation volume of V

$$L_{\mathrm{coil}} = \frac{\int_V (\mathbf{H} \cdot \mathbf{B})_{\mathrm{COMSOL}} \mathrm{d}V}{I_{\mathrm{s}}^2}; \quad \mathbf{H} = \mathbf{B}/\mu, \tag{38}$$

  where $\mu = \mu_{\mathrm{r}}\mu_0$ and μ_{r} is a material value of magnetic permeability ($\mu_{\mathrm{r}}^{\mathrm{Cu}} = \mu_{\mathrm{r}}^{\mathrm{W}} \doteq 1$ and $\mu_{\mathrm{r}}^{\mathrm{EUROFER\ 97}} = 40$ [43]) relative to vacuum $\mu_0 = 1.257 \times 10^{-6}$ H/m [8].

- Inductance of supply *stranded wire* cables was approximated as an inductance of twisted pair

$$L_{\mathrm{cable}} = (4 \times 10^{-7}[\mathrm{H/m}]) \cdot \ln\left(\frac{2s_{\mathrm{cable}}}{D_{\mathrm{cable}}}\right) \cdot d_{\mathrm{cable}} \quad [44], \tag{39}$$

  where we considered wire diameter D_{cable} to be the same as wire separating distance s_{cable}.

- The inductance of Capacitor Energy Storage (CES) $L_{\mathrm{CES}} = L_{\mathrm{switch}} + L_{\mathrm{capa}}$ is discussed below in Section 4.2.2 and is negligible compared to other values.

Also parasitic capacitance can arise on the cables themselves. The real conductor has a resistance, resistance creates a voltage drop and the voltage difference at the two ends of the conductor is actually a capacitor. The parasitic capacitance of the supply cables can

again be approximated by a twisted pair

$$C_{\text{cable}} = (28[\text{pF/m}]) \cdot \frac{\varepsilon_{\text{r}}}{\ln\left(\frac{2s_{\text{cable}}}{D_{\text{cable}}}\right)} \cdot d_{\text{cable}} \quad [44], \tag{40}$$

where ε_{r} is the material relative value of permittivity, which we set $\varepsilon_{\text{r}} = 1$, because we consider the coil and some part of the cable in a neutron radiation zone in a vacuum, where common insulating materials are not usable. We obtain values of 10^0 nF, which, as we shall see, are negligible to the capacity C_{CES}.

Before C_{CES}, we calculate the circuit resonant frequency f using inductive reactance X_{L}

$$X_{\text{L}} = 2\pi f L \quad \text{and} \quad U_{\text{L}} = I_{\text{s}} X_{\text{L}} \quad \rightarrow \quad f = \frac{U_{\text{L}}}{2\pi L I_{\text{s}}}, \tag{41}$$

where we consider for voltage on the inductor $U_{\text{L}} = U_{\text{CES}}$. We then calculate C_{CES} in order to fit the resonant frequency

$$C_{\text{CES}} = \frac{1}{L \cdot (2\pi f)^2} \tag{42}$$

The remaining parameter is the circuit ohmic resistance $R = R_{\text{Cu}} + R_{\text{eddy}} + R_{\text{CES}}$. Similarly to L, we calculate it as the sum of three resistive components:

- Resistance of the coil and cable R_{Cu} can be determined from their geometry, because, as we will show later in Section 4.2.1, the ratio of ohmic resistance for AC and DC current is $R_{\text{AC}}/R_{\text{DC}} = 1$.

- The largest losses ($\approx 10\times$ larger than the rest) are found in the conductive surroundings of the coil (especially AMC), which are caused by eddy currents. In COMSOL Multiphysics, we calculated the mean value of surroundings resistance R_{COMSOL}, which we then scaled to any frequency f as

$$R_{\text{eddy}} = R_{\text{COMSOL}} \cdot \sqrt{\left(\frac{f}{f_{\text{COMSOL}}}\right)} \tag{43}$$

- And again resistance of switches and capacitors $R_{\text{switch}} + R_{\text{capa}} = R_{\text{CES}}$ is discussed in the Section 4.2 below.

Now we can calculate total ohmic losses of the sweeping system of $2 \times N$ coils per one ELM. Because, in fact,

$$I_{\text{s}}(t) = I_{\text{s0}} \sin(2\pi f \cdot t) \cdot \exp(-t \cdot \frac{2R}{L}) \tag{44}$$

we have to integrate the losses over τ_{ELM}

$$E_{\Omega}^{\mathrm{ELM}} = \int_0^{\tau_{\mathrm{ELM}}} \frac{1}{2} R[I_{\mathrm{s}}(t)]^2 \mathrm{d}t \cdot \tau_{\mathrm{ELM}} \cdot 2 \cdot N \tag{45}$$

We estimated the ELM time scale $\tau_{\mathrm{ELM}} = 3$ ms based on scaling in [28], which results to a very similar time scale as on ITER. Dissipated energy from CES per one ELM can be evaluated as

$$E_{\mathrm{diss}}^{\mathrm{ELM}} = \frac{E_{\Omega}^{\mathrm{ELM}}}{\frac{1}{2} C_{\mathrm{CES}} U_{\mathrm{CES}}^2} \cdot \tau_{\mathrm{ELM}} \cdot 100[\%], \tag{46}$$

where We studied $E_{\mathrm{diss}}^{\mathrm{ELM}}$ in order to reduce the sweep amplitude λ_{sweep} during ELM. Because $I_{\mathrm{s}}(t) \sim \sin(2\pi f \cdot t)$, the *strike-point* stays at the sweep edges longer than in the middle position (the *sine* function changes the fastest when equals to zero) which yields undesirably low F_{STS}. However, even when $\lambda_{\mathrm{sweep}} \sim I_{\mathrm{s}}$ is reduced to $0.7 \cdot I_{\mathrm{s0}}$ (for $N_{\mathrm{turns}} = 63$), the Heat Conduction simulation [37] concludes that this effect is unfortunately negligible.

Finally, the dependence of F_{STS} on N_{turns} is estimated by fitting the Heat Conduction simulation results [37] as

$$F_{\mathrm{STS}} = 1 + \frac{3}{4} \ln(1 + f \cdot \tau_{\mathrm{ELM}}) \sqrt{\lambda_{\mathrm{scaled}} / \lambda_{\mathrm{q}}^{\mathrm{ELM}}}, \tag{47}$$

where $\lambda_{\mathrm{q}}^{\mathrm{ELM}} = 2$ cm is the EU DEMO ELM divertor heat flux decay length scaled in [28]. But λ_{sweep} cannot be set directly into Eq. 47, because, as we stated earlier in Section 3.4, there is a bond between the sweeping circuit and the eddy currents due to which $\lambda_{\mathrm{sweep}} \sim N_{\mathrm{turns}} \cdot I_{\mathrm{s}}$ does fully not apply. λ_{sweep} needs to be fixed at higher frequencies as

AC voltage amplitude U_{CES}	±18 kV
AC current amplitude I_{s}	±16 kA
Strike-point sweep amplitude λ_{sweep}	±5 cm
Length of connection cables d_{cable}	100 m
Divertor hole diameter (toroidal, poloidal)	10 cm, 30 cm
EU DEMO ELM decay time τ^{ELM}	3 ms
EU DEMO ELM divertor decay length $\lambda_{\mathrm{q}}^{\mathrm{ELM}}$	2 cm
Capacitor Energy Storage capacitance C_{CES}	77 µF
Total inductance L	99 µH
Sweeping frequency f	1.8 kHz
Ohmic losses per ELM $E_{\Omega}^{\mathrm{ELM}}$ for all coils	140 kJ
Weight of two coils and their cables $M_{\mathrm{coil}} + M_{\mathrm{cable}}$	5.2 t
Relative energy dissipation within one ELM $E_{\mathrm{diss}}^{\mathrm{ELM}}$	20 %
Surface Temperature Suppression Factor F_{STS}	3.2

Table 2: *Parameters of the sweeping system parameterized for the EU DEMO fusion tokamak. Two coils and cable is in each 54 divertor cassettes. The values are for $N_{turns} = 63$, for which the highest $F_{STS} = 3.2$ was reached.*

$$\lambda_{\text{scaled}} = \lambda_{\text{sweep}} \cdot \exp(-f/2.4\text{kHz}) \tag{48}$$

We plotted the resulting dependencies in Figure 25.

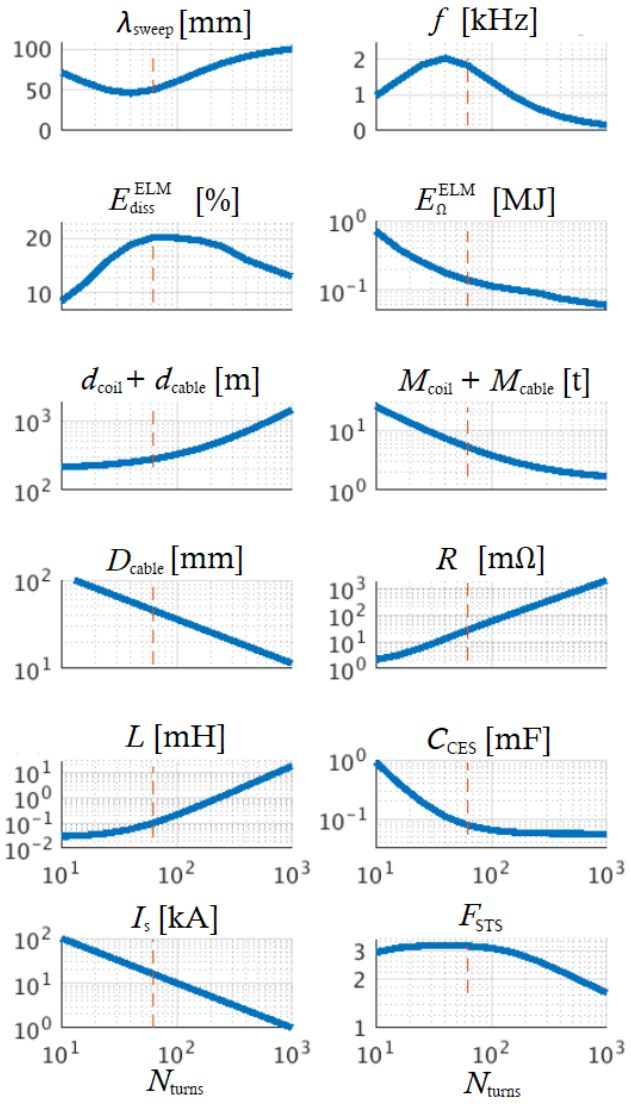

Figure 25: *Scan over number of turns per coil N_{turns}. Highest Surface Temperature Suppression Factor $F_{STS} = 3.2$ is reached for $N_{turns} = 63$. Obtained and modified from [37].*

In Figure 25 we can see that for higher number of turns $N_{\text{turns}} > 100$, the connection to the capacitor plays negligible role, however, F_{STS} drops due to smaller resonant frequency f. For $N_{\text{turns}} < 50$, the ohmic heating loss E_{Ω}^{ELM} and total mass $M_{\text{coil}} + M_{\text{cable}}$ rise to unacceptable large values. The highest F_{STS} whilst still low E_{Ω}^{ELM} is reached $N_{\text{turns}} \approx 60$, for which the crucial system parameters are summarized in Table 2. Thanks to these simple graphs, we were able to realize that the only parameter we should really maximize is the capacitor voltage U_{CES}. Thanks to the simulations from [37] we see that, unfortunately,

F_{STS} rises only very weakly with voltage as $F_{\mathrm{STS}} \sim \sqrt[3]{U_{\mathrm{CES}}}$.

We consider all the coils connected as fully independent circuits due to safety: if several of them break down, the system still works, with just proportionally lower amplitude. Another option would be to connect them all parallel into a single and much bigger capacitor bank. However, our market search concluded that such a big CES would anyway sustain from a similar amount of components (if CES is composed only from market available products), thus its complexity would not yield any advantage.

4.2 Feasibility

4.2.1 Stranded wires

Litz wire technology has been known since the first radio transmissions on medium frequencies ($\sim$ 1 MHz). The trick is the way the wires are wounded. The result of these winding patterns is to equalize the proportion of the overall length over which each strand is at outside of the conductor. This has an effect of distributing the current equally among the wire strands, reducing its resistance, see Figure 26. In other words, at higher frequencies, as with AMC, the current density only accumulates on the conductor surface. Because the cable consists of several conductors, it is possible to change positions of outer and inner conductors along the cable. This minimizes the inductance of the cable and spreads the current density over the entire cable cross-section.

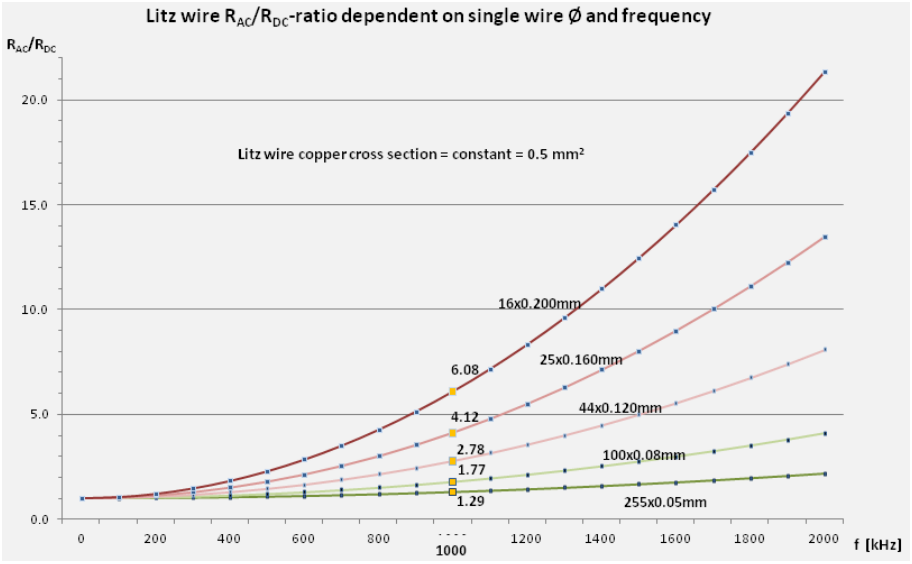

Figure 26: *Dependence of the resistance ratio when alternating current is applied R_{AC} and when direct current is applied RDC on AC frequency for different wire diameter. $R_{AC}/R_{DC} > 1$, due to eddy currents, which drive the current density to the surface of the cable (reduces the effective cross section, i.e. increases the resistance). Obtained from [45].*

Thanks to assumed 45 mm thick Litz-type conductor, its resistivity is low enough to

dissipate only 60% of capacitor energy during one ELM. Litz wires with non-insulated strands (*non-insulated Litz wire = stranded wire*), which we consider as a necessary condition in neutron radiation environment, has 5× higher $R_{\mathrm{AC}}/R_{\mathrm{DC}}-1$ increase with frequency with respect to an insulated Litz wire, see Figure 27. At frequency below 100 kHz, however, $R_{\mathrm{AC}}/R_{\mathrm{DC}} \approx 1$ (see Figure 26). Therefore, at our frequency 1.8 kHz, we can simply $R_{\mathrm{AC}} = R_{\mathrm{DC}}$, assuming the strands are less then 0.25 mm thick.

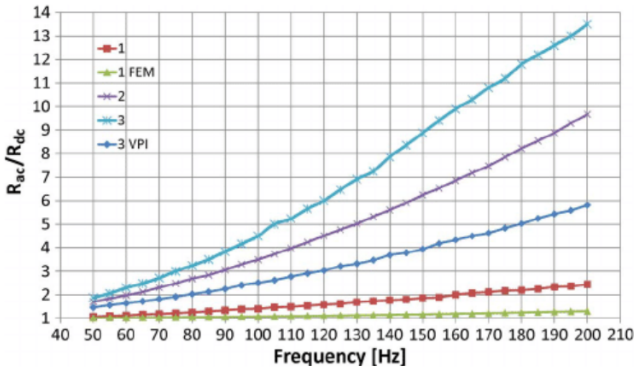

Figure 27: *Dependence of the resistance ratio when alternating current is applied R_{AC} and when direct current is applied RDC on AC frequency for different wire types. Type-1 means insulated strands, type-2 means oxidized strands and type-3 stands for non-insulated strands (FEM is a simulation that was tested in [46] and VPI is an additional method of impregnation, both of these graphs are not important for us). Obtained from [46].*

4.2.2 Capacitor banks

Performed analysis of the circuit and its influence on the *strike-point* sweeping showed us that capacity is the loosest parameter for us and is in the order of commonly available Capacitor Energy Storage (CES). So a standard non-polarized CES (which can, unlike other types, work in AC mode) will suffice. We know that $F_{\mathrm{STS}} \sim \sqrt[3]{U_{\mathrm{CES}}}$, so we would want the largest possible voltage U_{CES}. On the other hand, the dependence is so weak that we prefer to limit ourselves to a voltage of ~ 18 kV, at which there are still no undesirable problems with sparking in the circuit.

For the independent coil connection (connection, where every coil has its own CES), we can use, for example, a ring-film capacitors ($U_{\mathrm{capa}} = 8$ kV, $C_{\mathrm{capa}} = 50$ µF) [47] in series of $N^{\mathrm{s}}_{\mathrm{capa}} = 5$ in $N^{\mathrm{p}}_{\mathrm{capa}} = 10$ parallel channels. This yields a voltage of $U_{\mathrm{CES}} < N^{\mathrm{s}}_{\mathrm{capa}} \cdot U_{\mathrm{capa}} = 40$ DCkV= 20 ACkV with a capacity of $N^{\mathrm{p}}_{\mathrm{capa}} \cdot C_{\mathrm{capa}}/N^{\mathrm{s}}_{\mathrm{capa}} = 0.1$ mF, a parasitic resistance of $R_{\mathrm{capa}} = N^{\mathrm{s}}_{\mathrm{capa}} \cdot N^{\mathrm{p}}_{\mathrm{capa}} = 0.1$ mΩ and a parasitic inductance of $L_{\mathrm{capa}} = 25$ nH for a single coil. The resulting peak current through one capacitor $I_{\mathrm{capa}} = I_{\mathrm{s}}/N^{\mathrm{p}}_{\mathrm{capa}} = 1.6$ kA is acceptable for such capacitor. In total, it would be necessary to connect $N^{\mathrm{s}}_{\mathrm{capa}} \cdot N^{\mathrm{p}}_{\mathrm{capa}} \cdot N = 2,700$ capacitors (only to sweep the outer *strike-point*), thus a custom CES would be preferable option for such a huge project as EU DEMO1.

4.2.3 High power switches

For switching the voltages of U_{CES} and currents of I_{s}, typically thyristors and IGBT transistors are used. However, due to the difficulties with the thyristor turning off and insufficient pulse length, in our application IGBT transistors are more convenient. Since any available discrete semiconductor switches have still insufficient breakdown voltage and maximum current, we consider again a Series-Parallel ($N^{\mathrm{s}}_{\mathrm{switch}} = 15 \times N^{\mathrm{p}}_{\mathrm{switch}} = 6$) combination of IGBT transistors ($U_{\mathrm{switch}} = 1.2$ kV, $I_{\mathrm{switch}} = 3.6$ kA) [48] yields parameters over our requirements of $N^{\mathrm{s}}_{\mathrm{switch}} \cdot U_{\mathrm{switch}} = 18$ kV and a maximum continuous current of $N^{\mathrm{p}}_{\mathrm{switch}} \cdot I_{\mathrm{switch}} = 21.6$ kA.

Since the voltage drop is only $U^{\mathrm{ON}}_{\mathrm{switch}} = 2$ V for one ON switch, we get an effective resistance of $R_{\mathrm{switch}} = \frac{N^{\mathrm{s}}_{\mathrm{switch}} \cdot U^{\mathrm{ON}}_{\mathrm{switch}}}{N^{\mathrm{p}}_{\mathrm{switch}} \cdot I_{\mathrm{switch}}} = 1.4$ mΩ for one coil. IGBT is in principle a transistor, so for AC circuits at a resonant frequency, $N^{\mathrm{AC}}_{\mathrm{switch}} = 2$ opposing switches must be connected in the circuit, where each takes current in one direction. In total, the system requires $N \cdot N^{\mathrm{s}}_{\mathrm{switch}} \cdot N^{\mathrm{p}}_{\mathrm{switch}} \cdot N^{\mathrm{AC}}_{\mathrm{switch}} = 9,720$ IGBT transistors. We consider their parasitic capacitance to be negligible with respect to the capacitor, as well as the capacitor resistivity is negligible with respect to the switch.

An example of the feasibility of such a switching approach is the industrial pulsed power device presented in [49]. There, a similar block of IGBT transistors is utilized for periodical switching of 20 kV, 150 A pulses. Obviously, by a parallel combination of such blocks, the desired current could be reached.

5 Discussion

Since this is a completely new approach how to suppress ELM induced damage, several feasibility issues were not treated here due to its complexity and probably relatively low significance.

Even with a possible 1 Hz natural ELM frequency and an almost continuous EU DEMO mode, IGBT switches would turn ON/OFF $\sim 10^5$ times in one day. Older high-current switch technologies have only achieved such lifetime values, so the question is whether current and future technology or custom-made CES will achieve better qualities.

The magnetic field sum from the coils and the plasma equilibrium would not only generate linear perturbation (used for the 3D tracking) but also ergodic regions (with fully chaotic 3D topology) similar to the Resonant Magnetic Perturbation (RMP) technique. We think, however, that the ergodicity in our system is much weaker than in RMP because of:

1. much higher toroidal symmetry (number of coils $N = 54 \geq 2 + 2$ usually considered in RMP),

2. all the coils have the same polarity whilst in RMP the even/odd coils switch polarity,

3. RMP coils located at midplane integrate the chaotic perturbation over much longer distance than the swept coils in divertor.

Therefore, in this study we ignored the ergodicity issue.

There is a risk of possibly induced currents in the plasma by this oscillating magnetic field. In similar calculations for RMP [50], these plasma induced currents somehow reduce the RMP-field penetration into the plasma. We did not consider this issue due to its complexity and it should be investigated in follow up studies.

We also do not consider core plasma MHD instabilities which might be induced by this oscillating magnetic field, however, we think it is negligible because the perturbation is strongly localized within the divertor region.

In [51], significant neutron irradiation of 2-4 displacement/atom/year is expected in the region behind the water/helium cooled divertor cassette. There also nuclear heating of 5 MW/m^3 is calculated for EUROFER. Assuming similar values for the copper coils, it is comparable to the coil ohmic heating and thus requires attentive investigation in future studies.

If the frequency of ELMs was increased to safer $f_{\mathrm{ELM}} = 10$ Hz [52] (natural ELM 1 Hz) via additional ELM mitigation methods, we would get a continuous power of ohmic losses $E_{\Omega}^{\mathrm{ELM}} \cdot f_{\mathrm{ELM}} = 1.4$ MW which we consider still acceptable.

Finally, the question is whether this financially, technologically and energy-intensive system is worth a $F_{\mathrm{STS}} \doteq 3$ times lower PFC surface temperature, but we will probably find out when the situation demands it. What is certain is that the system can be further improved, such as finding a suitable method to simulate a better AMC (or limit AMC to the immediate vicinity of the coils as in Figure 23), designing a custom-made CES or even test completely different circuit connection (we chose the RLC circuit for its natural simplicity, but in terms of current technologies, similar oscillations can be excited by the external circuit and even not only harmonics).

6 Conclusion

We studied feasibility of a yet-never-tested technology aimed to suppress surface temperature rise during the undesired ELMs (possible to use only as an emergency system when other ELM-size control system fails) in EU DEMO1 divertor which are predicted to highly exceed tungsten damage threshold which would otherwise led to thermal cracking, melting and sputtering. The same principle would be applicable to other research or thermonuclear energy tokamaks when increasing and concentrating energy in the plasma, such as spARC (which will face the same or even worse heat loads) or COMPASS Upgrade [53].

The result of this work are the parameters of the system, which was now tested for the first time in the currently assumed magnetic and geometric configuration of EU DEMO1. Fast harmonic sweep of the outer *strike-point* would decrease the targets surface temperature by factor of three. It requires installation of a dedicated in-vessel 1.5 tons copper coils inside each 54 divertor cassettes (2 coils in order to sweep also both inner and outer target), each in a resonant circuit with 18 kV capacitor bank and an array of IGBT units, requiring power supply of 140 kJ per ELM. This technology can be usefully combined with other ELM-suppression methods (resonant magnetic perturbation and impurity seeding), however, not with liquid metals.

References

[1] L. Paraquez, et. al.: *Shale Gas in the United States: Transforming Energy Security in the Twenty-first Century*. Norteamérica. 10. 7-38. (2014), https://doi.org/10.20999/nam.2015.a001.

[2] C. Lai, et. al.: *Global warming and the mining of oceanic methane hydrate*. Topics in Catalysis. 32. 95-99. (2005), https://doi.org/10.1007/s11244-005-2879-4.

[3] S. Entler, et al.: *Approximation of the economy of fusion energy*. Energy 152 (2018) 489: https://doi.org/10.1016/j.energy.2018.03.130

[4] International Thermonuclear Experimental Reactor: *The ITER tokamak*. [online], [cited 1.3.2022], Available from: https://www.iter.org/

[5] EUROfusion: *European Research Roadmap to the Realisation of Fusion Energy, Long Version*. [online], [cited 12.4.2022], Available from: https://www.euro-fusion.org/fileadmin/user_upload/EUROfusion/Documents/2018_Research_roadmap_long_version_01.pdf

[6] G. Federici, et. al.: *The EU DEMO staged design approach in the Pre-Concept Design Phase*. Fusion Engineering and Design 173 (2021) 112959: https://doi.org/10.1016/j.fusengdes.2021.112959

[7] O. Semerak: *Speciální teorie relativity*. Script for the lecture of the same name at FMP of Charles University, Prague 2012

[8] Physical Measurement Laboratory of NIST: *International System of Units*. [online], [cit. 23.4.2022], Dostupné z: https://physics.nist.gov/cuu/Constants/index.html

[9] B. Sedlak: *Elektřina a magnetismus*. Script for the lecture of the same name at FNSPE of Czech Technical University, Prague 2002

[10] I. Stoll: *Mechanika*. Script for the lecture of the same name at FNSPE of Czech Technical University, Prague 2010

[11] A.W. Leonard, et. al.: *Edge-localized-modes in tokamaks*. Physics of Plasmas 21, 090501 (2014): https://doi.org/10.1063/1.4894742

[12] M. Hron, et al.: *Overview of the COMPASS results*, 2021 Nucl. Fusion in press: https://doi.org/10.1088/1741-4326/ac301f

[13] J. Horacek: *Horacek Res.Prof. thesis: long A4 version*. [online], [cited 22.3.2022], Available from: https://www.researchgate.net/publication/336375260_Horacek_ResProf_thesis_long_A4_version

[14] J. Horacek, et. al.: *Plans for Liquid Metal Divertor in Tokamak Compass*. Plasma Physics Reports volume 44, pages652–656 (2018)

[15] F. Maviglia, et. al.: *Impact of plasma-wall interaction and exhaust on the EU-DEMO design*. Nuclear Materials and Energy 26 (2021) 100897: https://doi.org/10.1016/j.nme.2020.100897

[16] A. Hassanein, et. al.: *Vertical displacement events: A serious concern in future ITER operation*. Fusion Engineering and Design 83(7-9):1020-1024 (2008): http://dx.doi.org/10.1016/j.fusengdes.2008.05.032

[17] R. Wenninger, et. al.: *DEMO Exhaust Challenges Beyond ITER*. European Physical Society Conference on Plasma Physics P4.110 June 2015, Lisbon, Portugal

[18] G. Pintsuk, et. al.: *Qualification and post-mortem characterization of tungsten mock-ups exposed to cyclic high heat flux loading*. Fusion Eng. Des. 88 (2013) 1858–1861: https://doi.org/10.1016/j.fusengdes.2013.05.091

[19] T. Putterich, et. al.: *Calculation and experimental test of the cooling factor of tungsten*. Nucl. Fusion 50 025012 (2010): http://dx.doi.org/10.1088/0029-5515/50/2/025012

[20] T.E. Evans, et. al.: *RMP ELM suppression in DIII-D plasmas with ITER similar shapes and collisionalities*. Nuclear Fusion 48(2):024002 (2008): http://dx.doi.org/10.1088/0029-5515/48/2/024002

[21] L. Baylor, et. al.: *ELM mitigation with pellet ELM triggering and implications for PFCs and plasma performance in ITER*. Journal of Nuclear Materials, 463, 104–108 (2015): http://dx.doi.org/10.1016/j.jnucmat.2014.09.070

[22] E. Luna, et. al.: *Understanding the physics of ELM pacing via vertical kicks in JET in view of ITER*. Nuclear Fusion 56(2):026001 (2016): http://dx.doi.org/10.1088/0029-5515/56/2/026001

[23] G. Federici, et. al.: *Overview of the DEMO staged design approach in Europe*. Nucl. Fusion 59 066013 (2019): http://dx.doi.org/10.1088/1741-4326/ab1178

[24] J. Horacek, et. al.: *Modeling of COMPASS tokamak divertor liquid metal experiments*. Nuclear Materials and Energy 25:100860 (2020): https://doi.org/10.1016/j.nme.2020.100860

[25] J. Horacek, et. al.: *Predictive modelling of liquid metal divertor: from COMPASS tokamak towards Upgrade*. Phys. Scr. 96 124013 (2021): https://doi.org/10.1088/1402-4896/AC1DC9

[26] Fusion for Energy: *Europe and Japan complete JT-60SA, the most powerful tokamak in the world!*. [online], [cited 13.4.2022], Available from: https://fusionforenergy.europa.eu/news/europe-and-japan-complete-jt-60sa-the-most-powerful-tokamak-in-the-world/

[27] G. Federici, et. al.: *Assessment of erosion of the ITER divertor targets during type I ELMs*. Plasma Phys. and Contr. Fus. 45 (2003) 1523-1547: http://dx.doi.org/10.1088/0741-3335/45/9/301

[28] J. Horacek, et. al.: *Feasibility study of fast swept divertor strike point suppressing transient heat fluxes in big tokamaks*. Fusion Eng. Des., 123, 646-649 (2017): https://doi.org/10.1016/j.fusengdes.2017.01.027

[29] R. Duban: *Study of New Technique for Distribution of Tokamak Divertor Plasma Heat Flux by Fast Swept Magnetic Coil*. Master's thesis, Czech Technical University, FNSPE, Prague, 2017

[30] J. Horacek, et. al.: *Conceptual study of fast swept divertor strike point suppressing transient heat fluxes in DEMO tokamak*. 27th Symposium on Plasma Physics and Technology, June 20 - June 23, 2016, CVUT, FEL, Prague, Czech Republic (2016)

[31] J. Horacek, et. al.: *Conceptual study of fast-swept divertor strike points suppressing ELM heat flux*. SOFT 2016: Symposium on Fusion Technology /29./. Prague, 05.09.2016-09.09.2016

[32] V. Sedmidubsky: *Fyzika termojaderného plazmatu v tokamaku*. Student's project, Jan Neruda Grammar School, Prague, 2017

[33] J. Horacek, et. al.: *Suppressing ELM heat in big tokamaks by fast swept divertor strike point*. European Physical Society Conference on Plasma Physics P2.126 June 2017, Belfast, Ireland

[34] S. A. Silburn, et. al.: *Mitigation of divertor heat loads by strike point sweeping in high power JET discharges*. Phys. Scr. 2017 014040: http://dx.doi.org/10.1088/1402-4896/aa8db1

[35] F. Maviglia, et. al.: *Limitations of transient power loads on DEMO and analysis of mitigation techniques*. Fusion Eng. Des., 109–111, Part B, 1067-1071 (2020): https://doi.org/10.1016/j.fusengdes.2016.01.023

[36] A. Q. Kuang, et. al.: *Divertor heat flux challenge and mitigation in SPARC*. Journal of Plasma Physics, 86(5), 865860505 (2020): https://doi.org/10.1017/S0022377820001117

[37] J. Horacek, et. al.: *New concept suppressing plasma heat pulses in a tokamak by fast divertor sweeping*. Submitted to Nature Physics, (2022).

[38] S. Lukes, et. al.: *Využití jevu vířivých proudů k usměrnění vysokofrekvenčního magnetického pole*. [online], [cited 1.3.2022], Available from: http://golem.fjfi.cvut.cz/wiki/TrainingCourses/FTTF/2020-2021/SamuelLuk/index

[39] K. Hashemi: *Derivation of the Skin Effect*. [online], [cited 1.3.2022], Brandeis University, Available from: http://www.bndhep.net/Lab/Derivations/Skin_Effect.html

[40] F. Hernandez, et. al.: *First principles review of options for tritium breeder and neutron multiplier materials for breeding blankets in fusion reactors*. Fusion Engineering and Design. 137. 243-256 (2018): https://doi.org/10.1016/j.fusengdes.2018.09.014

[41] J.P. Gunn, et. al.: *Surface heat loads on the ITER divertor vertical targets*. 2017 Nucl. Fusion 57 046025: https://doi.org/10.1088/1741-4326/aa5e2a

[42] J. Adamek, et. al.: *On the transport of edge localized mode filaments in the tokamak scrape-off layer*. Nuclear Fusion 60 (2020) 096014: http://dx.doi.org/10.1088/1741-4326/ab9e14

[43] K. Mergia, et al.: *Structural, thermal, electrical and magnetic propertiesof Eurofer 97 steel*, Journal of Nuclear Materials 373 (2008) 1–8: https://doi:10.1016/j.jnucmat.2007.03.267

[44] All About Circuits: *Twisted-Pair Impedance Calculator*. [online], [cited 26.4.2022], Available from: https://www.allaboutcircuits.com/tools/twisted-pair-impedance-calculator/

[45] ELEKTRISOLA Dr. Gerd Schildbach GmbH & Co KG: *Calculation of High Frequency Litz Wire Losses*. [online], [cited 20.4.2022], Available from: https://www.elektrisola.com/en-us/Litz-Wire/Info#calculation-of-high-frequency-litz-wire-losses

[46] H. Hamalainen, et. al.: *AC Resistance Factor of Litz-Wire Windings Used in Low-Voltage High-Power Generators*. IEEE Transactions on Industrial Electronics, 61. 693-700 (2014): http://dx.doi.org/10.1109/TIE.2013.2251735

[47] Pulse Power and Measurement Ltd (PPM): *PRODUCT DATA SHEETS, 775D506980-106 Power Ring*. [online], [cited 20.4.2022], Available from: https://advanced-conversion.com/wp-content/uploads/2021/03/powerring-775D106-march2021-web.pdf

[48] Infineon Technologies AG: *IGBT Modules, FZ3600R12HP4*. [online], [cited 20.4.2022], Available from: https://www.infineon.com/dgdl/Infineon-FZ3600R12HP4-DS-v02_03-EN.pdf?fileId=db3a3043163797a601165742504207c7

[49] M. Gaudreau, et. al.: *Solid-State Power Systems for Pulsed Electric Field (PEF) Processing*. Pulsed Power Conference, 2005 IEEE: http://dx.doi.org/10.1109/PPC.2005.300605

[50] M. Becoulet, et. al.: *Screening of resonant magnetic perturbations by flows in tokamaks*. 2012 Nucl. Fusion 52 054003: http://dx.doi.org/10.1088/0029-5515/52/5/054003

[51] J.H. You, et. al.: *Progress in the initial design activities for the European DEMO divertor: Subproject "Cassette"*. Fusion Engineering and Design 124 (2017) 364–370: https://doi.org/10.1016/j.fusengdes.2017.03.018

[52] R.A. Pitts, et. al.: *Physics basis for the first ITER tungsten divertor*. Materials and Energy, vol. 20, 586 100696 (2019): https://doi.org/10.1016/j.nme.2019.100696

[53] S. Lukes, et al.: *Conceptual design of reciprocating probes and material-testing manipulator for tokamak COMPASS Upgrade*. Journal of Instrumentation, 17(02), C02007 (2022): https://doi.org/10.1088/1748-0221/17/02/c02007